DEVELOPMENT AND APPLICATION OF THE STOKES TRAP FOR MEASUREMENT OF INTERPARTICLE INTERACTIONS

BY

ANISH SHENOY

DISSERTATION

Submitted in partial fulfillment of the requirements
for the degree of Doctor of Philosophy in Mechanical Engineering
in the Graduate College of the
University of Illinois at Urbana-Champaign, 2017

Urbana, Illinois

Doctoral Committee:

Professor Sascha Hilgenfeldt, Chair
Associate Professor Charles M. Schroeder, Director of Research
Professor Christopher V. Rao
Assistant Professor Qian Chen

Abstract

The ability to trap and control single particles in free solution has led to major advances in science and engineering. Common methods for particle trapping and manipulation often rely on optical, magnetic, acoustic, or electric forces. However, the vast majority of these methods critically depend on the target particle possessing specific physical properties such as index of refraction or surface charge. In this research, we have designed and built a Stokes trap, which allows for the manipulation and control of an arbitrary number of arbitrary type particles using only fluid flow. In this way, we have effectively constructed a 'smart microfluidic device' by coupling feedback control with microfluidics, thereby enabling new routes for the fluidic-directed assembly of particles. This work is comprised of three distinct but interrelated efforts towards the precision trapping and manipulation of multiple particles using fluid flow. In the first project, the control algorithm for a microfluidic process is extensively studied for confining a single particle in solution. Here, we study the response of trapped particles actuated using a combination of proportional, integral, and derivative controllers (PID control), which extends beyond our prior work where we utilized a simple proportional controller for 2-D manipulation of particles in free solution. We investigate the effect of controller gains, flow rate, and feedback response times on the robustness of trapping, using a combination of simulation and experimental studies. In the second project, we present the development and application of the Stokes Trap, which is a multiplexed microfluidic method for arbitrary manipulation of an arbitrary number of particles in solution. We demonstrate simultaneous manipulation of two particles in a simple microfluidic device, and also achieve fluidic directed assembly of multiple particles in solution. In the third project, the Stokes trap is used to implement and experimentally demonstrate trajectory control using fluidic

trapping, wherein particles are controlled by a path-following framework that improves the precision and the speed of manipulation of particles along arbitrary paths. An extended Kalman filter is also implemented, which effectively reduces the offset due to unmodeled phenomena during particle trapping. Finally, these techniques are leveraged to demonstrate the direct determination of solvent-mediated hydrodynamic interactions (HI) between two freely suspended colloidal particles in flow. From a broad perspective, this work provides a robust framework for studying fundamental interactions between particles or for guiding the directed assembly of materials.

To my family and friends.

Acknowledgments

I would first like to thank my primary advisor, Prof. Charles M. Schroeder. Charles has been incredibly supportive when pursuing difficult projects and I've benefited greatly from his perspective on research and mentorship over the last few years. Prof. Sascha Hilgenfeldt has been instrumental in helping me to develop a mindset of tackling complex problems using a first principles approach. I would like to thank Prof. Chris Rao for numerous discussions and advice on the control systems related aspects of my project. I also thank Prof. Qian Chen for serving on my doctoral committee and providing valuable feedback.

I am also grateful for the privilege of working with highly talented scientists in the Schroeder research group. They've helped me out at various points during my Ph.D. by not only being available for discussing research ideas but also by creating a fun and entertaining atmosphere in the lab. I would like to thank all the previous group members - Melikhan, Chris, Arnab, Eric, Folarin, Amanda, Utsav, Danielle, Luke, Dan and Kejia. Thanks are also due to current group members Kaiwen, Peter, Songsong, Bo, Lawrence, Shivani, Dinesh, Michael, Yi and Subha - I've enjoyed working with all of you, and I've also enjoyed our numerous lab excursions to downtown Champaign.

Finally, I would like to thank my parents for their love, support and encouragement and my friends Arun, Arka, Subhro, Shashank, Abhijith and Shishir for ensuring that there was never a dull moment in Champaign.

Table of Contents

List of Figures

Chapter 1

Introduction

In recent years, techniques for confining and manipulating particles have ushered in a revolution in the natural and applied sciences. Nearly all techniques rely on a set of fundamental forces to confine particles and molecules over long timescales, including those that rely on optical fields [1–4], magnetic fields [5, 6], electrical fields [7–11], acoustical fields [12, 13] and fluid flow fields [14–18]. To this end, these techniques have been used with remarkable success in diverse fields ranging from biology to nanotechnology, such as for cellular chromosome manipulation [19], observing shape fluctuations of single DNA molecules in free solution [20], and cooling of atoms to low temperatures [1].

The underlying mechanism of trapping provides a natural basis for classifying these techniques into passive (non-feedback control based) and active (feedback control based) trapping methods. Passive traps confine particles in stable potential wells. Any incoming disturbance that displaces the particle leads to a restoring force which returns the particle back to the equilibrium point. The shape of the potential can also be tuned to control the magnitude of the restoring force. As a consequence, feedback control is not required to confine particles over long time periods. Examples of passive traps include optical traps and magnetic traps. On the other hand, active traps require feedback control to stabilize a particle at the desired location. The feedback control is necessary either to cancel the thermal motion of a particle suspended in a solvent, as in the electrokinetic traps or the Stokes trap, or it can be used to stabilize a particle at a non-stable equilibrium point, as in the automated hydrodynamic trap. For example, Fig. 1.1 shows a particle in a saddle point potential that is to be confined at a target position. The saddle point is a potential energy minima in one direction, and a maxima in the other direction, as shown in Fig. 1.1.

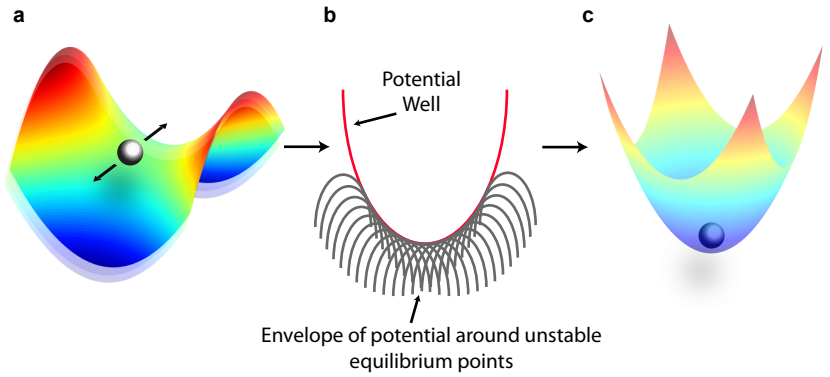

Figure 1.1: The feedback driven motion of a saddle point potential up and down along the unstable axis stabilizes a particle at the desired location. (a) A particle is to be stabilized at a desired location by moving the saddle point along the unstable axis. (b) The envelope of the potential at several different positions of the unstable equilibrium point creates an effective potential well centered on the target location. (c) The particle is trapped in the resulting potential well.

The particle is thus stable along the direction along which the potential is a minima (the stable axis) and unstable along the direction where the potential is a maxima (the unstable axis). In this case, the feedback control moves the saddle point along the unstable axis, as shown in Fig. 1.1a. The motion of the saddle point potential results in an effective potential well as shown in Fig. 1.1b, and the particle is finally confined in the resulting potential well (Fig. 1.1c). Active methods thus are fundamentally limited in their response since calculating and applying the feedback control for a given position of a particle is not instantaneous, and is associated with a finite delay. On the other hand, the application of feedback control makes it possible to study new phenomenon which were hitherto inaccessible. Furthermore, since the applied feedback control is meant to stabilize only the particle of interest, these techniques also facilitate selectively trapping particles, in comparison to passive traps, which need a dilute solution to ensure that only a single particle is trapped in a potential well.

Despite being widely adopted, not all techniques offer the same flexibility vis-à-vis the properties of particles that can be trapped. Table 1.1 compares three techniques for trapping. Although optical trapping is able to access a wide range of forces, the application of a

Table 1.1: Comparison of trapping methods. For a more detailed table, see [10].

	Hydrodynamic trap	**Optical Trap**	**Electrokinetic trap**
Method	Hydrodynamic flow	Focused laser beam	Electroosmotic + Electrokinetic flow
Implementation	Simple microfluidic device	Complex, expensive equipment	Electrodes + high fields/gradients
Force range	1 fN - 1 pN	0.1 fN - 100 pN	up to 20 pN
Force scaling	$\sim R$	$\sim R^3$	$\sim R$
Restrictions on particle or buffer properties	No	Refractive index of the particle must be greater than the buffer	The buffer must have mobile ions
Isolation from crowded media	Yes	No	Yes

focused laser beam is accompanied by localized heating which is ill suited for trapping biological entities [21]. Additionally, the force scales as the third power of the particle radius, which means that the force decreases by three orders of magnitude when the particle radius decreases by a factor of 10. Optical trapping also requires specialized equipment to develop tightly focused laser beams. Electrokinetic traps have a favorable scaling behavior with respect to the applied force, but still apply high electric field gradients to manipulate particles. Finally, hydrodynamic trapping not only exhibits a favorable scaling behavior for the force but also confines particles using the gentle action of fluid flow. It requires a simple microfluidic device for confining particles and does not impose any restrictions on the properties of the particle or the surrounding medium. From this perspective, hydrodynamic trapping offers a distinct advantage compared to the other two trapping methods.

In 1934, G. I. Taylor developed the first active trap based on hydrodynamic flow [22]. The four-roll mill was able to confine single macroscopic particles or immiscible droplets by continuous rotation of four cylinders, thereby generating a stagnation point flow. The

original four-roll mill relied on manual (human) feedback control for particle confinement, which limits precision and controllability. In 1986, Bentley and Leal developed an automated four-roll mill by controlling the rotational speeds of the rollers using a computer [23]. The automated four-roll mill, however, was based on a 'macrofluidic' experimental flow cell, which complicates the confinement of small particles due to finite system response times. In recent years, the advent of microfluidics has allowed for the fabrication of flow devices with small feature sizes, thereby enabling dynamic fluidic control with correspondingly small timescales. In 2003, a microfluidic cross-slot device was used to trap single DNA molecules near the stagnation point of a planar extensional flow, albeit using manual (tedious) human control over hydrostatic pressure in the outlet flow channels [24,25]. A microfluidic four-roll mill was also developed and shown to generate extensional, rotational, and linear mixed flows [26,27], however, these devices lack feedback control, which precludes long-term confinement of single particles and molecules.

In 2010, Schroeder and coworkers built and demonstrated an automated hydrodynamic trap capable of confining single particles at a target position for several minutes in a PDMS-based microfluidic device [14]. In this device, an on-chip membrane valve was used to modulate flow rate in one outlet channel, thereby enabling particle trapping near a stagnation point for long times [15]. By incorporating multiple on-chip valves, it was shown that single particles can be precisely manipulated in two-dimensions using the sole action of fluid flow [16]. The automated hydrodynamic trap relies on proportional control for particle manipulation which was sufficient for precise confinement of small particles in solution (*e.g.* 500 nm particles confined to within 180 nm of a setpoint position).

Although proportional control was sufficient for confining single particles, we wanted to investigate if we could improve the tightness of confinement by adopting a different controller. Simultaneously, it was imperative to understand how experimental parameters such as the stiffness of the valve, the viscosity of the solvent and the speed of feedback influenced the ability to trap a particle of a given size. We were also intrigued by the possibility of

simultaneously manipulating several particles and investigating the interactions between a pair of freely suspended particles, mediated only by the solvent. This dissertation describes our efforts to answer these pertinent questions.

1.1 Dissertation overview

Prior versions of the hydrodynamic trap employed a proportional controller without a systematic study of the control schemes, gain constants, or system parameters. However, robust confinement of the particle over long time scales requires an in depth understanding of how controller parameters such as the controller gain, and the experimental parameters such as viscosity, strain rate, and particle diameter, affect the performance of the hydrodynamic trap. In Chapter 2, a control model for the hydrodynamic trap is developed, and the performance of the trap under varying combinations of proportional-integral-derivative (PID) controllers is studied. The control model enables a simulation of the trapping behavior across a wide range of solvent viscosities, particle diameters, temperatures and strain rates. Here, the effects of each component of the PID controller are systematically considered by varying the controller gains experimentally.

Although the automated hydrodynamic trap is able to effectively confine a single particle in a tight region around the target position, this method was inherently limited to trapping a single particle. Chapter 3 describes the development of the Stokes trap, which is a new method for the multiplexed manipulation of particles using fluid flow. The Stokes trap benefits from the several advantages of the hydrodynamic trap while also enabling studies of interactions between two suspended particles, such as cell adhesion and droplet coalescence. Here, we implement a model predictive control (MPC) algorithm that calculates optimal flow rates for manipulating an arbitrary number of particles. Moreover, modeling errors in the system model lead to an offset during particle trapping, which was reduced using an integrator. We demonstrate a significant improvement over the tightness of confinement

of the automated hydrodynamic trap, the precise manipulation of two particles along an arbitrary path, and the assembly of a simple structure by trapping two sticky particles and bringing them together to link them.

Chapter 3 describes the implementation of a model predictive control (MPC) formulation, which allows for the precise manipulation of particles along a preprogrammed path, wherein, the setpoint is stepped along the path without any consideration of the position of the particle. In Chapter 4, an extended Kalman filter is used to estimate an arbitrary unknown disturbance and to simultaneously cancel it, thereby achieving a reduced offset. The model predictive control problem is reformulated for trajectory control, which amounts to a path following scheme that coordinates the motion of the set point with the motion of the particle. This reformulation leads to a significant improvement in the path following speed compared to original implementation. These two features are combined together to estimate the velocity field induced by solvent-mediated hydrodynamic interactions between two freely suspended particles.

Finally, in Chapter 5, the main research contributions of this dissertation are summarized, and future extensions and applications of the Stokes trap are discussed.

Chapter 2

A control based model for analyzing the automated hydrodynamic trap[1]

The automated hydrodynamic trap developed by Schroeder and coworkers [16] enables the precise 2-D positioning and manipulation of micro and nano-scale particles using the sole action of fluidic forces. This setup employs a simple linear feedback controller without a systematic study of the control schemes, gain constants, or system parameters. However, robust confinement of particles over long time scales critically requires a clear understanding of the effect of the controller and system parameters on the stability of trapped particles. For example, in the macroscopic computer controlled four-roll mill [23], it was reported that trapping was difficult to achieve using P and PD control, owing to slow response times of the fluid and the measurement delay.

In this chapter, we implement three different control schemes for hydrodynamic trapping, including a proportional (P), a proportional-integral (PI), and a proportional-derivative (PD) controller. We study the effect of controller gain constants on the stability of trapped particles. In addition, we develop a control-based model to characterize the response of the hydrodynamic trap, and we use this model to simulate the stability of trapped particles over a wide range of response times and Péclet numbers. In this way, we use a combination of experiments and simulations to provide a clear understanding of the effect of feedback controllers and system parameters on trap performance, which will facilitate the development of improved controllers for robust trapping under variable system conditions.

[1]This work was published in A. Shenoy, M. Tanyeri, C.M. Schroeder, "Characterizing the performance of the hydrodynamic trap using a control-based approach", *Microfluidics and Nanofluidics*, **18**, 1055-1066 (2015)

2.1 Hydrodynamic Trap: Trapping Mechanism

The hydrodynamic trap is based on the active feedback control of a stagnation point flow generated at the cross-slot junction of a two-layer PDMS-based microfluidic device (Fig. 2.1). In the fluidic layer, fluid enters the cross-slot through two opposing inlet streams and exits through two perpendicular outlet streams, as shown in Fig. 2.1b. A control layer is positioned above the fluidic layer and consists of a pneumatic valve situated above one of the outlet streams. Control is achieved by the actuation of the integrated membrane valve on the device. In this setup, the flow field in the cross-slot consists of a compressional axis along the inlet direction and an extensional axis along the outlet direction, with no rotational flow characteristics. This flow pattern is known as a planar extensional flow and contains a stagnation point (a point with zero velocity) in the cross-slot region. The local fluid velocity in the vicinity of the stagnation point depends on the relative distance from the stagnation point, so we can express the velocity at a point (x, y)as a superposition of velocities along the extensional and compressional flow directions:

$$\begin{aligned} \vec{v}(x,y) &= \vec{v}_{ext}(y) + \vec{v}_{comp}(x) \\ \vec{v}_{ext}(y) &= \dot{\varepsilon}(y - y_s)\hat{j} \\ \vec{v}_{comp}(x) &= -\dot{\varepsilon}(x - x_s)\hat{i} \end{aligned} \tag{2.1}$$

where $\hat{i}$ and $\hat{j}$ are unit vectors along the compressional and extensional axes respectively, $\dot{\varepsilon}$ is the strain rate, and (x_s, y_s) is the stagnation point position. The flow field is characterized by a set of hyperbolic streamlines within the cross-slot junction.

From the velocity field, it can be inferred that a particle is attracted towards the stagnation point along the compressional axis and repelled from the stagnation point along the extensional axis. In this work, we consider 1D particle trapping at arbitrary points along the principal axis of extension in planar extensional flow; in other words, we characterize trap

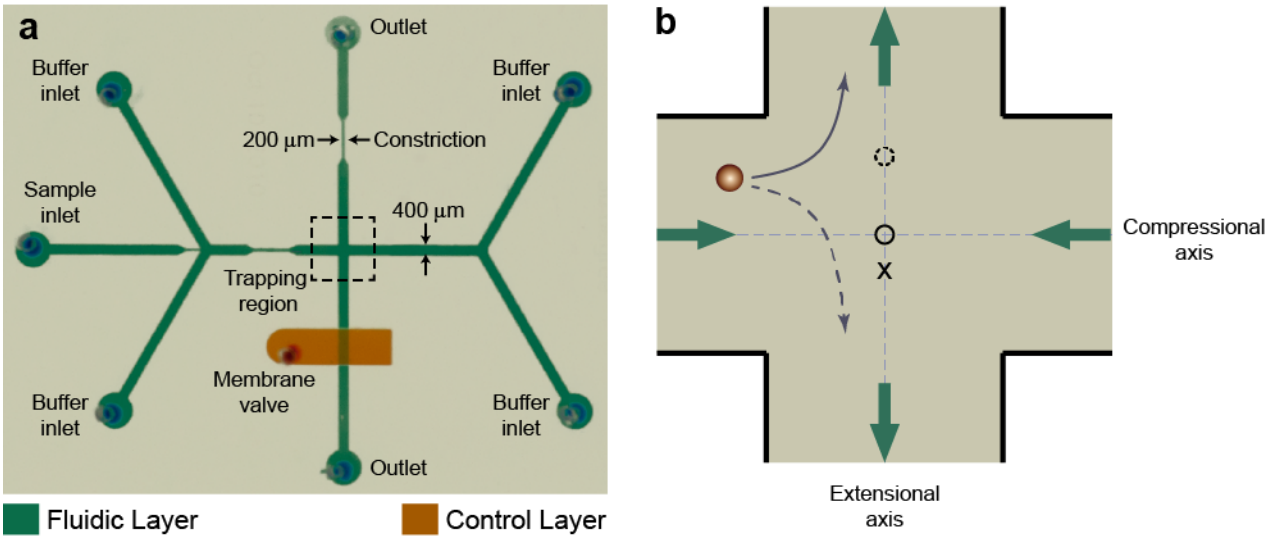

Figure 2.1: Microfluidic-based hydrodynamic trap. (a) Optical micrograph of the device. Particles are confined at a user-defined set point in the cross-slot junction (indicated by the dashed box). (b) Schematic of the cross-slot region and trap mechanism. Two inlet and two outlet streams are indicated by the thick arrows (green), x indicates the user-defined set point, the solid circle indicates the initial stagnation point position, and the solid arrow indicates the particle trajectory. To trap the particle, the stagnation point is translated along the extensional axis to a new position (shown by the dashed circle), which directs the particle toward the set point along a new trajectory (indicated by the dashed arrow). The origin is at the center of the cross-slot.

stability in along the unstable trapping direction (outflow direction). Due to the semi-stable nature of the trap potential, particles are stably confined along the compressional flow axis without the need for active feedback control in this direction. Therefore, the stagnation point is a stable equilibrium point along the compressional axis and an unstable equilibrium position along the extensional axis. From this view, it is clear that feedback control is necessary for particle trapping - for instance, in directing a particle towards the stagnation point in the y direction. Following the initial trapping phase, further disturbances due to Brownian motion and environmental noise necessitate the use of active feedback control for particle confinement.

The mechanism of hydrodynamic trapping has been previously described [14–16]; here, we briefly review it for clarity. Consider a freely suspended particle entering the cross-slot

junction (Fig. 2.1b) that is to be trapped at a user defined set point (indicated by the 'x' symbol). Without control, the particle would simply follow the trajectory (streamline) shown by the solid arrow. In order to trap the particle, the controller moves the stagnation point in the positive y direction instantaneously, which would tend to direct the particle to follow a new trajectory (shown by the dashed line) that will cause it to approach the set point. Next, the updated position of the particle is acquired and the process is repeated, continuously moving the stagnation point position along the extensional axis within the cross-slot.

The motion of the stagnation point is achieved by pressurization or de-pressurization of the integrated membrane valve (Fig. 2.1a). The movement of the valve enables a dynamic metering of the flow rate in the fluidic channel in the lower outlet stream. In this way, pressurizing the valve causes a constriction of the outlet channel under the valve, which increases the fluidic resistance, consequently decreasing fluid flow through the lower outlet channel and moving the stagnation point towards this channel. De-pressurization causes an analogous effect in the upper outlet flow channel. The overall control process consists of the following steps and is implemented using a LabVIEW program: (1) determining the centroid position of the particle by performing image acquisition and analysis of the camera feedback data, (2) calculating the offset error between the set point position and current position, and (3) translating the stagnation point in the $+y$ direction (or $-y$ direction) by de-pressurizing (or pressurizing) the valve using the control algorithm described in the Methods section. This process is analogous to the balancing of a pendulum in an inverted position, which is an unstable equilibrium point.

2.2 Hydrodynamic Trap: Control Model

As discussed previously, hydrodynamic traps based on cross-slot microfluidic devices require feedback control only for manipulating the position of a particle in the y-direction (along the extensional axis). Hence, we focus on developing a control model for only the

y-direction, since the x-direction is stable. Given a stagnation point position y_s, the velocity of a particle in the y-direction is given by:

$$\frac{dy}{dt} = \dot{\varepsilon}(y - y_s) \tag{2.2}$$

where $\dot{\varepsilon}$ is the strain rate, y is the particle position, and y_s is the current stagnation point position, where all positions are measured along the extensional axis.

There is a finite delay between setting a new stagnation point position on the computer versus the actual update of the stagnation point position via valve actuation on the microdevice. The movement of the stagnation point from its prior position to the new position can be modeled as a first order process:

$$\frac{dy_s}{dt} = \frac{1}{t_v}(y_{s,new} - y_s) \tag{2.3}$$

where $y_{s,new}$ is the new stagnation point position set by the controller and t_v is the system response time. Together, Eqs. (2.2) and (2.3) represent the uncontrolled system.

In this process, there is a second finite delay in acquiring and analyzing image data to determine a particle's position, which is defined as the measurement delay, t_m. Furthermore, the stagnation point has a limited range of movement due to physical constraints on the on-chip membrane valve, which is accounted for in the model. Finally, the particle's final position y_f is also influenced by Brownian motion, which can be modeled as:

$$y_f = y + y_b \tag{2.4}$$

Here, y_b is the magnitude of random thermal motion superposed on the mean flow position y at a single time step. Following the fluctuation-dissipation theorem, y_b is assumed to be a Gaussian-distributed random variable with zero mean value and a standard deviation given

by:

$$y_{b,std} = \sqrt{\frac{2k_bT}{3\pi\eta d}(t_m + t_v)} \tag{2.5}$$

where k_B is the Boltzmann constant, T is the absolute temperature, η is the viscosity, and d is the particle diameter. Also, t_m and t_v are the measurement delay and the system response times, respectively. The time scale in Eq. (2.5) results from the implementation of the control algorithm for trapping a particle of diameter d. In particular, the LabVIEW algorithm initiates the control process (characteristic time t_v), after which the camera and imaging system process and determine the new position of the particle (characteristic time t_m). Thus, between successive snapshots of a particle's position, a time equal to $(t_v + t_m)$ has elapsed, as shown in Eq. (2.5).

Following acquisition of an image and determination of particle position from image data, the error between the set point and the current particle position is calculated. The error is input to the controller, which outputs a control signal to the system. The relationship between the input and the output of the controller is:

$$Q = \underbrace{K_pP}_{\text{Proportional}} + \underbrace{K_i\int_0^t Pdt}_{\text{Integral}} + \underbrace{K_d\frac{dP}{dt}}_{\text{Derivative}} \tag{2.6}$$

where P is the input and Q is the output. In the case of the control model, P is the offset error (distance) and Q is the position of the new stagnation point. In experiments, P is the offset error (distance) and Q is the voltage applied to the pressure transducer controlling the on-chip membrane valve, though it should be noted that the experimental controller does not use the exact form described in Eq. (2.6). In Eq. (2.6), K_p is the proportional gain constant, K_i is the integral gain constant, and K_d is the derivative gain constant. For implementing a proportional-only (P) controller, K_i and K_d are set to zero, for a proportional-integral (PI) controller K_d is set to zero, and finally for a proportional-derivative (PD) controller, K_i is

set to zero.

To facilitate analysis, parameters are converted to dimensionless forms by choosing the particle diameter d and the diffusion time $t_{diff} = 3\pi\eta d^3/4k_BT$ as the characteristic length and time scales, respectively. In this way, dimensionless parameters are denoted by variables with overbars and defined in the following way:

$$\overline{y} = \frac{y}{d},\ \overline{y}_s = \frac{y_s}{d},\ \overline{y}_{s,new} = \frac{y_{s,new}}{d},$$
$$\bar{t} = \frac{t}{t_{diff}},\quad \tau_v = \frac{t_v}{t_{diff}},\ \tau_m = \frac{t_m}{t_{diff}},$$

The particle Péclet number Pe is defined as the ratio of the diffusive time scale of the particle t_{diff} to the convective time scale $\dot{\varepsilon}^{-1}$:

$$Pe = \frac{t_{diff}}{t_{conv}} = \frac{3\pi\dot{\varepsilon}d^3}{4k_BT} \tag{2.7}$$

Using the characteristic length and time scales, Eq. (2.2), Eq. (2.3), and Eq. (2.5) are recast in dimensionless form:

$$\frac{d\overline{y}}{d\bar{t}} = Pe(y - y_s) \tag{2.8}$$
$$\frac{d\overline{y}_s}{d\bar{t}} = \frac{1}{\tau_v}(\overline{y}_{s,new} - \overline{y}_s) \tag{2.9}$$
$$\overline{y}_{b,std} = \sqrt{\frac{\tau_m + \tau_v}{2}} \tag{2.10}$$

where τ_m and τ_v are the dimensionless system response time and measurement delay.

To facilitate a control-based analysis of system response, we use Laplace transforms of the above equations to define transfer functions, assuming zero initial conditions. For Eq. (2.8)

and Eq. (2.9), the transfer functions are:

$$\begin{aligned} \frac{Y(s)}{W(s)} &= G_p = \frac{Pe}{Pe - s} \\ \frac{W(s)}{Z(s)} &= G_v = \frac{1}{\tau_v s + 1} \end{aligned} \tag{2.11}$$

where s is the Laplace domain variable and $W(s)$ and $Z(s)$ are the Laplace transforms of $\overline{y}_s$ and $\overline{y}_{s,new}$, respectively. If $P(s)$ and $Q(s)$ are the input and output quantities, then transfer functions for the time delay and the controller are given by the following equations:

$$\frac{Q(s)}{P(s)} = e^{-s\tau_m} \tag{2.12}$$

$$\frac{Q(s)}{P(s)} = K_p + \frac{1}{s}(K_i t_{diff}) + \frac{K_d}{t_{diff}} s \tag{2.13}$$

A block diagram of the control model is shown in Fig. 2.2. In general, we simulate the response of the system to a step change in offset error (or, analogously, particle position). We use this model to study the effect of variation of the controller parameters (K_p, K_i, K_d), and system parameters (Pe, τ_m , τ_v) on the stability of trapped particles. Using dimensionless system parameters allows us to capture the effects of a change in several dimensional parameters. For example, a variation in Péclet number can represent a change in particle diameter, a change in viscosity, a change in the strain rate, or any combination of these factors.

2.3 Methods & Materials

2.3.1 Device Fabrication

The hydrodynamic trap consists of a two-layer poly(dimethyl siloxane) (PDMS) device mounted on a glass coverslip, which is fabricated using standard soft-lithography techniques. The fluidic layer, which contains the sample and the 6 buffer channels (4 inlets and 2 outlets),

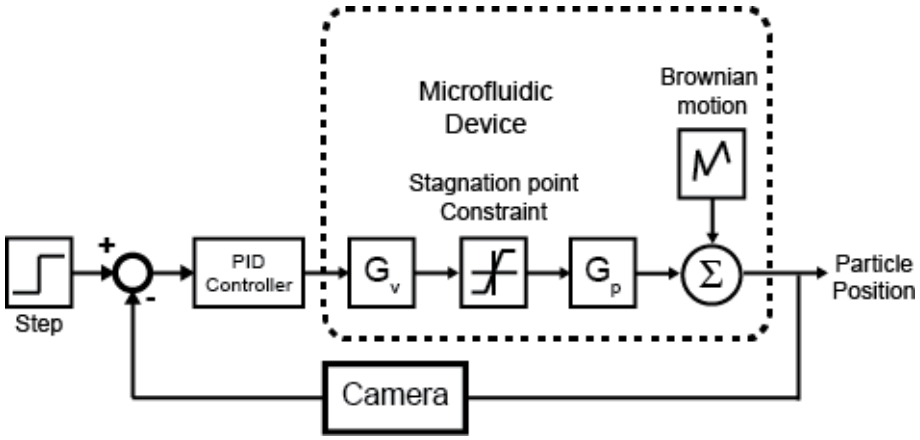

Figure 2.2: Block diagram showing the control model for the trap. The model includes the stagnation point constraint, Brownian motion, and the feedback delay due to image acquisition by a camera. The dashed box represents the uncontrolled microfluidic device.

is sandwiched between a glass cover slip and the control layer. The control layer consists of an elastomeric membrane valve positioned above one of the outlet channels. The sample is flow focused at the confluence of the two inlet channels and is delivered to the centre of the cross-slot junction. As described previously, pressurizing/de-pressurizing the membrane valve causes changes in the relative flow rates through the two outlets, thereby repositioning the stagnation point. In addition, the presence of a constriction in the other outlet necessitates a constant offset pressure in the valve to maintain the stagnation point at the centre of the cross-slot junction. This design allows the lower outlet channel to achieve a smaller fluidic resistance than the upper outlet channel, which allows for facile control of the stagnation point position about the centre of the cross-slot junction at finite pressures.

The fluidic and control layers are individually fabricated using replica molding. For both layers, a mold is prepared by spin-coating a thin layer ($\sim$ 70 µm) of negative photoresist (SU-8) onto a 3″ diameter silicon wafer, followed by UV exposure using a high-resolution transparency film as a mask. Molds are then developed using propylene glycol methyl ether acetate (PGMEA). For replica molding, the PDMS-based mold layers are treated with trichloro (1H, 1H, 2H, 2H-perfluorooctyl) silane vapor to facilitate straightforward peeling

and removal of the PDMS layer. The fluidic layer is fabricated by spin-coating PDMS having a 15:1 (w/w) base : crosslinker ratio, yielding a 100 µm thick layer on the mold. The control layer is fabricated by directly pouring PDMS having a 5:1 (w/w) base : crosslinker ratio on the control layer mold. Next, both layers are partially baked at 65 °C, 12 minutes for the control layer and 20 minutes for the fluidic layer. Next, the thick control PDMS layer is peeled off, thoroughly cleaned using cleanroom tape, and then aligned and sealed onto the thin fluidic layer, followed by overnight baking at 65 °C to yield a monolithic slab. This slab is then peeled off the mold, and access holes are punched to inlets and outlets using a needle with a blunt tip. Finally, the PDMS slab is bonded to a glass coverslip using plasma oxidation to obtain a functional device.

2.3.2 Experimental Setup

The microfluidic device is mounted on the stage of an inverted microscope (Olympus IX71) equipped with a 10x objective lens and a CCD camera. The four buffer inlets on the microdevice are connected to a single syringe mounted on a syringe pump (Harvard Apparatus) in order to maintain equal flow rates through all inlets. A separate syringe pump drives the flow for the sample inlet stream. The buffer solution is a glycerol-water solution with a viscosity of 0.0126 Pa-s at 298 K. The valve is pressurized using an electronic pressure transducer (Proportion Air) connected to a computer. A custom LabVIEW program developed for automated trapping coordinates image acquisition from the camera and regulates the pressure on the on-chip valve. The program performs the following steps: (i) acquires data from the camera to identify particles in the region of interest near the set point, (ii) identifies the particle closest to the set point by comparing the distances of the particles' center of mass to the set point, (iii) calculates the offset error between the set point and particle position for the selected particle, (iv) calculates the current control signal (in volts) and communicates this signal with the pressure transducer to translate the position of the stagnation point, and (v) repeats this process to minimize the error in order to maintain a

particle near the set point position. The image acquisition rate of the camera was 30 Hz throughout the experiments.

The LabVIEW program actuates the pressure transducer by transmitting an electrical signal (voltage) to the regulator. The voltage for actuating the transducer is calculated for each time step following a general PID controller:

$$\begin{aligned} Err_i &= Y_i - SP \\ V_i &= V_{i-1} \pm \left[K_P Err_i + K_i \sum_{k=0}^{i} Err_k \Delta t \right] + \frac{K_d}{\Delta t}(Err_i - Err_{i-1}) \end{aligned} \tag{2.14}$$

where Y_i is the current particle position along the extensional axis, SP is the set point, Err_i is the error between the set point and particle position, V_i is the updated voltage for the pressure transducer, K_p is the proportional gain constant, K_i is the integral gain constant, K_d is the differential gain constant, and Δt is the loop iteration time in LabVIEW, which is determined by the image acquisition rate of the camera. The loop iteration time is equal to the sum of the measurement delay and system response time. However, in our experiments, the system response time was generally small compared to the measurement delay time for a trapped particle, because minute changes in pressure are required to maintain a trapped particle near the set point. Hence, the loop iteration time reported by LabVIEW was roughly the same as the measurement delay (33 ms).

This algorithm is used because the position of the stagnation point is generally unknown in experiments, and the particle must be stabilized with the sole knowledge of the error between its current position and the set point. In addition, the relative distance between the particle and stagnation point is generally not known *a priori*, but this value can determined in real-time using the rate of change of error. In brief, we explain the set of decision criteria for determining the identity of the $\pm$ in Eq. (2.14) and determining the required voltage change. For calculating the error, all vertical distances (along the extensional axis) are measured from the top edge of the frame of the video (i.e., the origin defining $y = 0$ is at

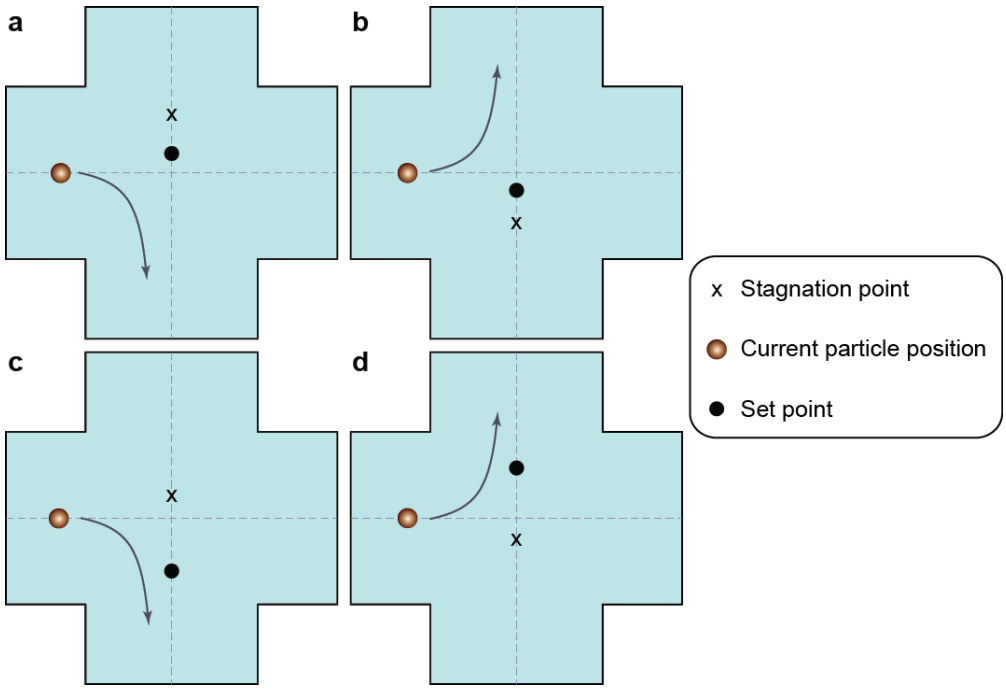

Figure 2.3: Schematic illustrating the four possible cases for carrying out the PID control based on the relative positions of the stagnation point, particle position, and set point.

the top of an image).

Based on the relative positions of the stagnation point, the particle, and the set point, there are four possible cases, as depicted in Fig. 2.3. Consider Fig. 2.3a, with the particle following a trajectory towards the lower outlet stream. Initially, the set point position lies between the stagnation point and the particle, and the flow advects the particle further away from the set point, so the present error will be larger than the previous value of the error. In this case, by increasing the voltage (and pressure) the stagnation point can be translated below the particle position (i.e., moving the stagnation point in the $+y$ direction), so that

Table 2.1: Control decision for four possible cases of relative error.

Case	**Error vs. Previous Error**	**Error $\lessgtr$0**	**Voltage increased/decreased**
A	$\|Error\| > \|Prev.Error\|$	Error>0	Increased
B	$\|Error\| > \|Prev.Error\|$	Error<0	Decreased
C	$\|Error\| < \|Prev.Error\|$	Error<0	Increased
D	$\|Error\| < \|Prev.Error\|$	Error>0	Decreased

the particle follows a trajectory towards the upper outlet, and hence towards the fixed set point. Based on this reasoning, a set of decision criteria can be developed to decide on whether to increase or decrease the voltage (and therefore the pressure) for each case. Once this is known, the magnitude of the increase/decrease is calculated using Eq. (2.14). This process is carried out at each time step, the particular case is identified, and then both the sign and the magnitude of change in the transducer voltage are calculated and implemented. The control decisions for all four cases in Fig. 2.3 are summarized in Table 2.1.

For studying the effect of the controller gains, 2.2 µm diameter fluorescent beads (SPHERO fluorescent particles, Nile Red, Spherotech Inc., IL) are trapped at specific buffer and sample flow rates and proportional gain K_p. The buffer is treated with a surfactant (0.05% v/v Triton-X), which minimizes aggregation of the beads. Next, a series of step changes in the particle position is applied to the system, with each step having a magnitude of 5 pixels and a duration of 40 seconds. In this way, a predefined constant time period step is applied to the trapped bead for 4 successive steps, and its response is recorded using the LabVIEW program. Application of a series of steps for a given set of parameters allows for multiple experiments to be performed in a single run. The standard deviation of particle position in the last 10 seconds of each step is calculated and is used as a metric to assess trap performance and stability. The time period is chosen such that it is sufficiently larger than the characteristic diffusion time of the particle, and data towards the end of the step is generally analyzed to suppress start-up or initial transient effects in the particle trajectories. This process is used for all steps in a single run, and the mean and standard deviation of the standard deviation values for each step in a run is calculated.

2.4 Results and Discussion

2.4.1 Experimental Results

2.4.1.1 P Controller: Effect of proportional gain, K_p

A proportional-only (P) controller is implemented by setting K_i and K_d to zero. For these experiments, we apply a series of periodic step changes, with each step having a magnitude of 5 pixels or ∼4.95 µm and of duration 40 seconds. The duration of the step change was chosen to be large enough so that all the transients had damped out. During each step, we maintain a constant value of Kp and sample and buffer flow rates. Following each step change, we track the response of the trapped particle. In addition, we also vary the proportional gain K_p and monitor particle trajectories for different K_p values. Subsequently, this process is repeated for different buffer flow rates. Fig. 2.4 shows the trajectory of a trapped particle during a series of step changes in the set point for a fixed flow rate and different values of K_p. Upon increasing the proportional gain K_p, the magnitude of position fluctuations for a trapped particle are suppressed to values smaller than the particle diameter (Figs. Fig. 2.4a-d).

Fig. 2.5 shows the standard deviation of particle position as a function of proportional controller gain K_p and sample flow rate. A proportional controller accounts only for the instantaneous offset error when calculating the control signal; therefore, increasing K_p allows the stagnation point to move more aggressively in order to minimize the perturbations of a trapped particle. From Fig. 2.5, it is apparent that larger values of K_p result in a smaller tightness of confinement for a trapped particle. However, above a certain limit, further increases in K_p will overcompensate for the error, thereby resulting in particle 'ringing' oscillations. For the conditions shown in Fig. 2.5a, we generally observed particle 'ringing' for values of $K_p > 0.030$.

In addition, an increase in the flow rate causes a particle to be advected over larger distances in the same amount of time. Given a constant feedback rate and gain constant, it

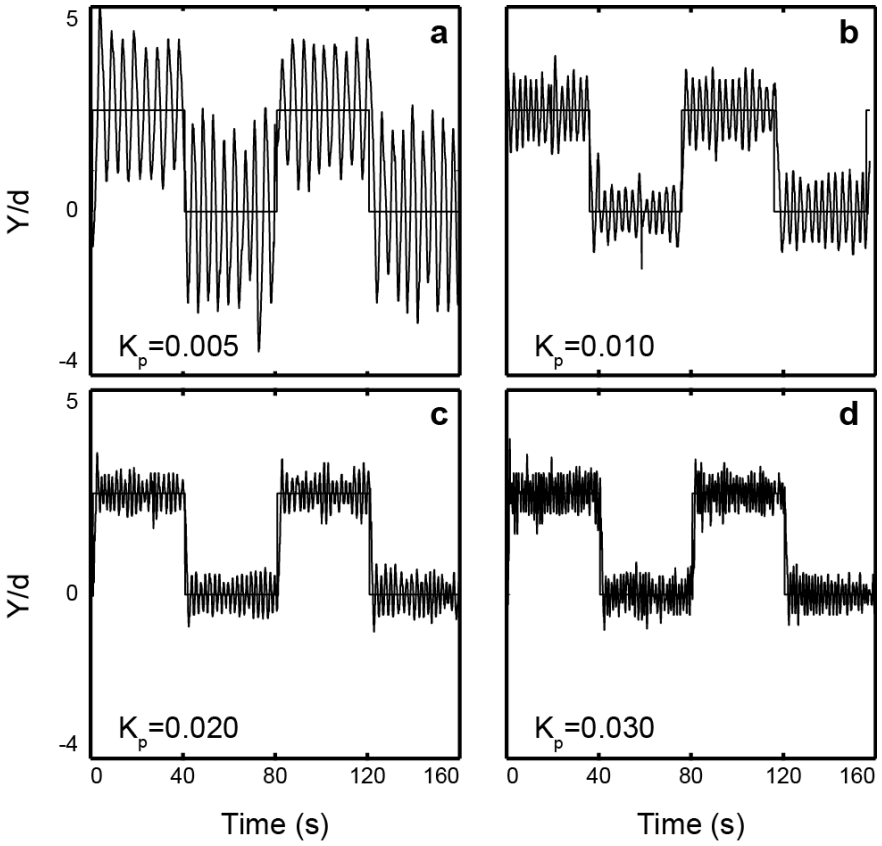

Figure 2.4: Experimental trajectories of trapped particle position for a P controller. In all cases, a 2.2 µm diameter particle is subjected to a step change of duration 40 s in set point position (constant flow rate of 30 µl h^{-1} and 5 µl h^{-1} for the buffer and sample, respectively). From (a) to (d), the proportional gain was increased from 0.005 to 0.030.

follows that the controller would need to correct for larger errors in a particle's trajectory. Therefore, for a constant controller gain K_p, the magnitude of particle position fluctuations increases upon increasing the flow rate. As shown in Fig. 2.5, particle position fluctuations increase in magnitude upon increasing the flow rate from 20 µl h^{-1} to 40 µl h^{-1} for small values of K_p.

2.4.1.2 PI Controller: Effect of integral gain, K_i

In a second set of experiments, we implemented a PI controller by setting $K_d = 0$ in Eq. (2.14). The integral gain constant K_i was varied over a fairly wide range of values for constant values of K_p and the flow rate. This process was repeated for a few sets of K_p

values.

Overall, we observed that adding an integral controller does not result in an improvement in the tightness of confinement vis-á-vis a simple P controller, as shown in Fig. 2.6a. Upon implementing integral control and varying K_i over a range of values, the magnitude of particle position fluctuations is not improved within statistically significant values. Differences between the magnitude of fluctuations for different K_p values are primarily attributed to the increased stabilization provided by the higher K_p value alone, as evidenced in Fig. 2.5.

Integral controllers are commonly used to correct constant offset errors present in the control variable, which cannot be corrected by using a P controller alone. In this experiment, there is no constant offset error when a simple P controller is used. In addition, the integral term in Eq. (2.14) does not contribute significantly to the controller output because the standard deviation is calculated over the final 10 seconds of a step, when particles tend to fluctuate around the set point position. As a result, essentially no significant improvement is observed by introducing an integral controller into this process.

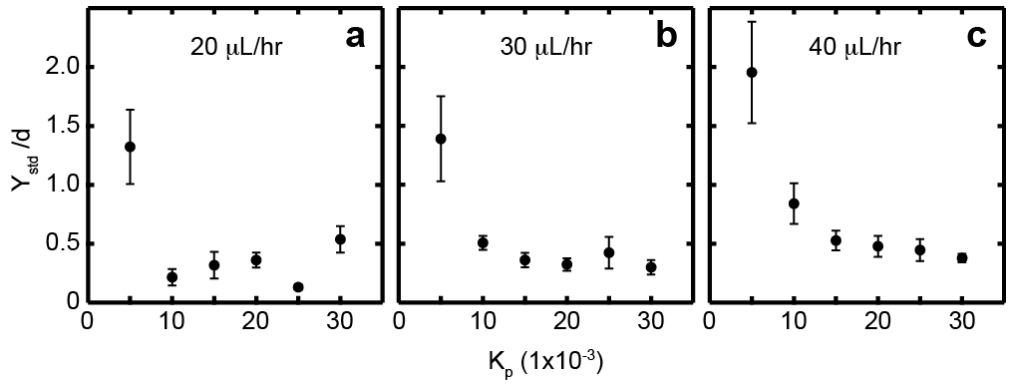

Figure 2.5: Experimental data showing response of a trapped particle as a function of K_p and flow rate using a P controller. Standard deviation of trapped particle position is shown. The buffer flow rate is increased from (a) 20 µl h^{-1}, (b) 30 µl h^{-1}, and (c) 40 µl h^{-1}.

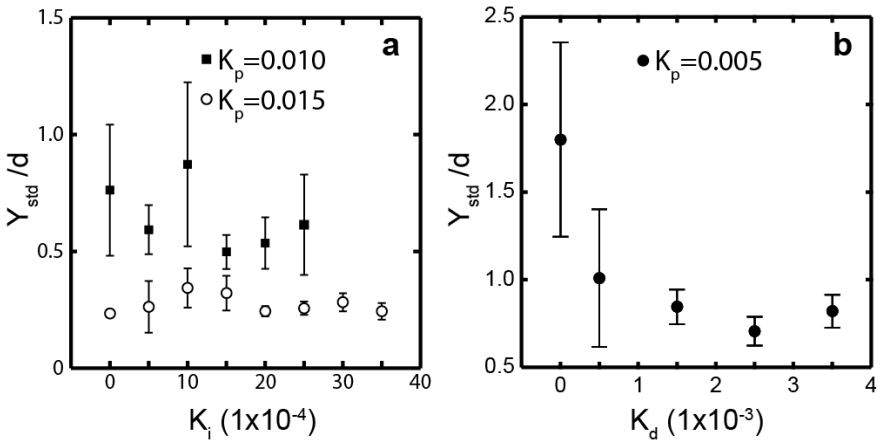

Figure 2.6: Experimental data showing response of a trapped particle as a function of: (a) K_i using a PI controller with constant K_p (K_d set to 0) and (b) K_d using a PD controller with constant K_p (K_i set to 0). Standard deviation of trapped particle position is shown. The experimental parameters are: a) sample flow rate 10 µl h^{-1}, buffer flow rate 10 µl h^{-1}, 30 second step duration; b) sample flow rate 5 µl h^{-1}, buffer flow rate 20 µl h^{-1}, 40 second step duration.

2.4.1.3 PD Controller: Effect of derivative gain, K_d

We further implemented a derivative controller for the hydrodynamic trap. Here, we consider the effect of derivative gain on the stability of a trapped particle by implementing a PD controller, as shown in Fig. 2.6. The derivative gain K_d was varied, while setting K_i to zero and maintaining all other parameters constant. For these experiments, we did not include integral control based on the results obtained in Fig. 2.6a.

We observed that derivative control greatly stabilizes the position of a trapped particle and suppresses fluctuations to within a particle diameter for smaller values of K_p. Derivative controllers account for the rate of change of error, which corresponds to the particle velocity. In stochastic systems, such as for a trapped bead subject to Brownian motion, the position of a particle at later times depends only on current conditions and is independent of the prior history (in other words, a Markov process). Consequently, a controller that modulates its signal based on particle velocity effectively damps particle fluctuations. From this view, it follows that increases in the derivative gain K_d, which acts as a damping parameter, result

in decreases in particle fluctuations, as demonstrated by Fig. 2.6b.

On the other hand, large values of K_d can amplify noise that causes a sudden jump in particle position, such as fluctuations in the flow field. This is a significant limitation of a derivative controller, and therefore the value of K_d should be tuned to meet the constraints dictated by noise on one hand and stability on the other. In this work, we manually varied the value of K_d, based on the response of the particle to high and low values of Kd.

Furthermore, the PD controller can be also be used to negate the effects of an increase or decrease in the temperature, which would change the magnitude of Brownian fluctuations. For example, a 5 K increase in temperature (298 K - 303 K) would induce a 20% increase in the root-mean-square particle displacement as a result of an increase in the thermal fluctuations of the particle and a decrease in the viscosity of the buffer solution. Under these conditions, we can tune the P and D components together to effectively damp particle fluctuations.

2.4.2 Control Model and Simulation Results

2.4.2.1 Comparison to experimental results

We used a control model to further understand the performance of the hydrodynamic trap and to compare experimental results directly to the model. In the model, we set the system parameters identical to experimental conditions as described below. In the simulation, a constraint of $\pm$100 µm is imposed on the movement of the stagnation point, which closely captures experimental conditions. The control model is simulated using Simulink (MathWorks).

Fig. 2.7 compares an experimental particle trajectory (Fig. 2.7a) to results from the simulation (Fig. 2.7b). This simulation result was generated by setting the particle diameter to 2.2 µm, viscosity to 0.0126 Pa-s at 298 K, and a step size of $\sim$4.95 µm. The system response time is set to 5 ms (based on the time required to increase the pressure from 0 - 30 psi), and the measurement delay was chosen as 33 ms, which corresponds to the

camera frame rate in experiments. Both experimental and simulation results show similar amplitudes of particle fluctuations, but slightly different periods, which can be attributed to different implementations of the controller in the simulation and LabVIEW. The simulation uses a controller of the form prescribed in Eq. (2.6), whereas the LabVIEW program uses a controller implemented according to Eq. (2.14). The major difference between the two versions is that the position of the stagnation point is known explicitly in the control model, whereas in experiments, the stagnation point position is generally not known in real time. For this reason, particles are trapped in experiments using knowledge of the error between the current position and set point, as well as the rate at which this error grows. In addition, the control model has a steady state offset (when using a proportional-only controller) that is not present in the experiments due to the implementation of P-only control in the experimental system. We therefore added an integral control component in the control model to correct for the offset.

Using the control model, we simulated the effect of system response time τ_v, measurement delay τ_m, and particle Péclet number Pe on the stability of a trapped particle. Simulations were performed over a wide range of Pe and dimensionless measurement delays while keeping other parameters constant, and the standard deviation of the particle was determined, analogous to the procedure used for experiments.

Using this approach, we simulated the response of a small trapped particle (100 nm diameter) subjected to a large 75 µm step change in set point in a fluid of viscosity 0.001 Pa-s at 298 K. In this set of simulations, we assessed the ability of the system to respond to large magnitude disturbances, such that the change in set point was 750x larger than the particle diameter. The K_p, K_i, and K_d values in the simulation are set to -20, -1.5 and -1.4, respectively. Moreover, the dimensionless measurement delay was varied between 5 and 300, and the dimensionless system response time was varied between 5 and 100, which correspond to experimental values typically encountered for image acquisition and for the system response time, respectively. It should be noted that for certain parameter ranges, the

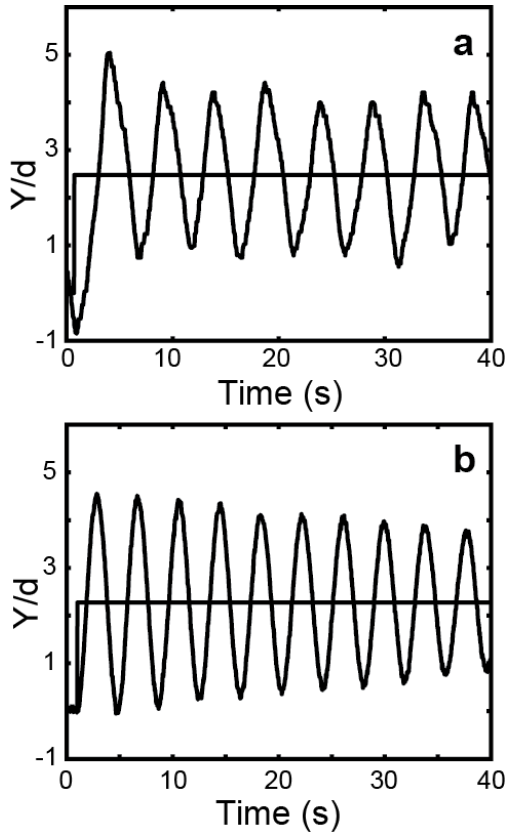

Figure 2.7: Response of a 2.2 µm trapped particle in (a) experiments and (b) simulations. In the experiment, the sample and buffer flow rates are 5 µl h^{-1} and 30 µl h^{-1}. In the simulation, $\dot{\varepsilon} = 0.26s^{-1}$, K_p = -1.5, and K_i = -10.

particle escaped the trap and the system was unstable; in this case, the standard deviation was set to a high value to differentiate it from stable parameter combinations (here it was set to 2.5).

We also simulate the response of the particle under experimental conditions (Fig. 2.9), with the particle diameter set to 2.2 µm, viscosity set to 0.0126 Pa-s and a step change of 4.95 µm.

2.4.2.2 Effect of measurement delay

For these simulations, the measurement delay was varied, while keeping the controller gains constant at the previously specified values, and the system response time set to 5 ms. Figure 2.8a shows a heat map illustrating trap stability (quantified as the standard deviation of particle position) as a function of Pe and dimensionless measurement delay. The deep red region represents parameter combinations that result in failing to trap the particle (an unstable system). The critical dimensionless measurement delay that causes a transition to instability remains constant across a wide range of particle Pe. Generally speaking, within the region of trap stability, the magnitude of particle fluctuations decreases upon increasing Pe. However, at very high Pe, the critical measurement delay decreases (not shown). This occurs because as the Pe increases, the camera needs to process image data faster to account for the increased rate of particle advection. Of course, the stability diagram shown in Figure 2.8 has been generated using a specific set of values for controller gains and step change; nevertheless, we have generated similar stability diagrams using a different parameter sets, and in all cases, the qualitative trend in the variation is similar.

For further insight, we also simulate the response of the particle under experimental conditions (Fig. 2.9a). Here, the particle is always within the accessible range of the stagnation point (i.e. particle displacement from the stagnation point is much less than 100 µm). Under these conditions we see that the particle is stably confined for the most of the parameter combinations; however at high Péclet numbers and measurement delays, an increase

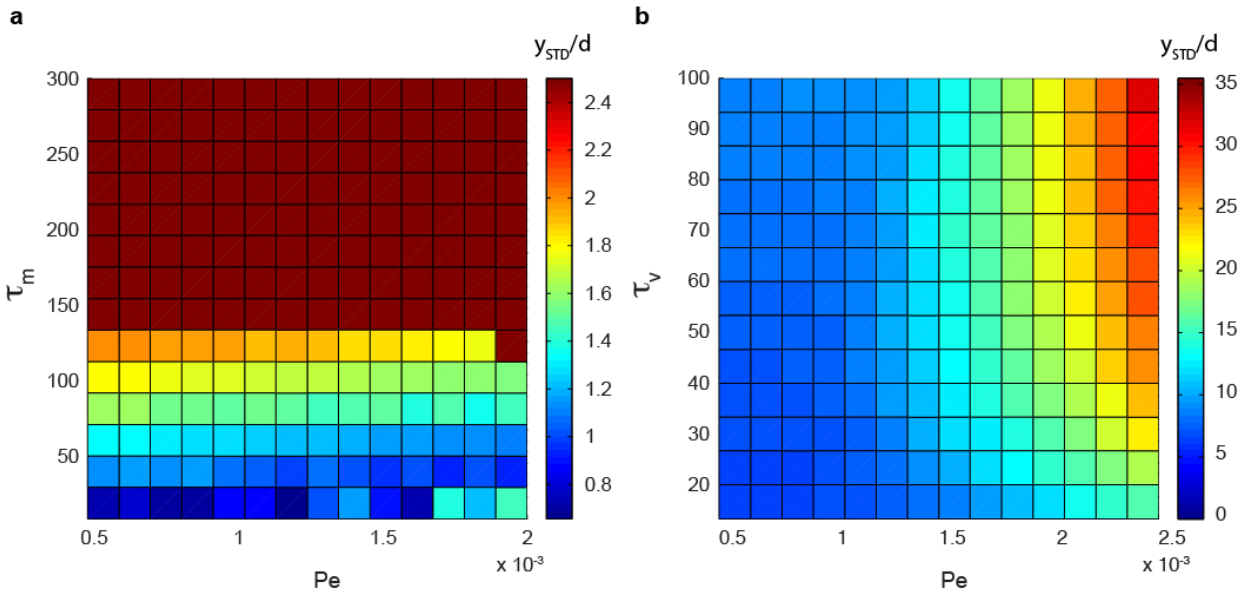

Figure 2.8: Simulations showing response of a trapped particle to measurement delay, system response time, and Pe. (a) Heat map showing standard deviation of trapped particle position as a function of Pe and dimensionless measurement delay. (b) Heat map showing standard deviation of trapped particle position as a function of Pe and dimensionless system response time. The parameter values are: for calculating diffusion time: η = 0.001 Pa-s, T = 298 K, d = 100 nm, Step: 75 µm; Controller gains: K_p = -20, K_i = -1.5, K_d = -1.4; a) τ_m varied from 5-300 with τ_v = 8.73 (corresponding to 5 ms), b) τ_v varied from 5-100 with τ_m =57.6 (corresponding to 33 ms).

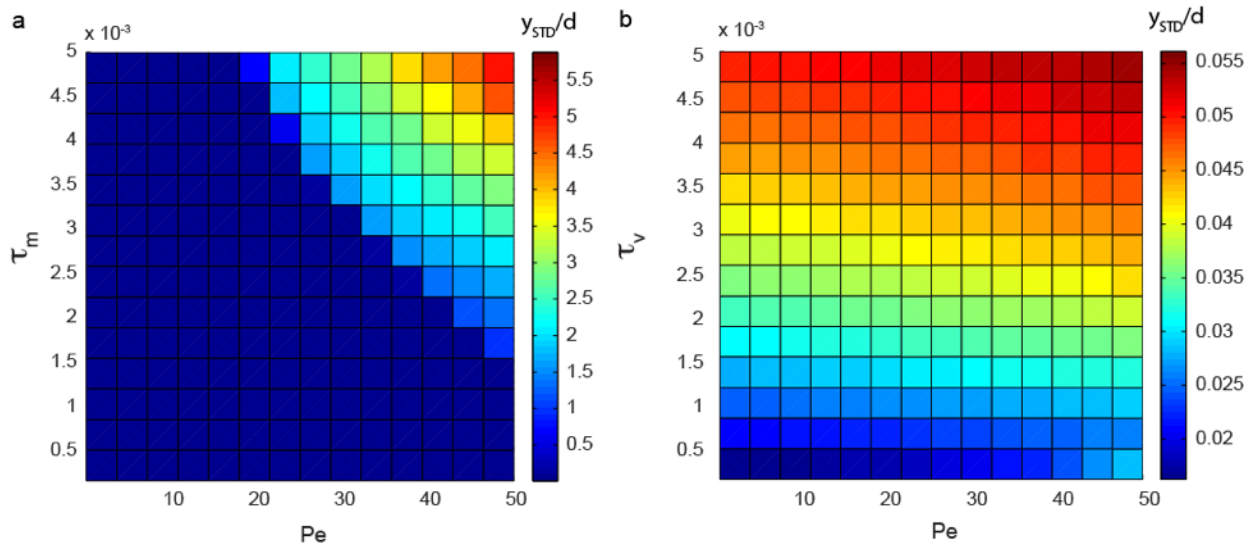

Figure 2.9: Simulations showing response of a trapped particle to measurement delay, system response time, and Pe. (a) Heat map showing standard deviation of trapped particle position as a function of Pe and dimensionless measurement delay. (b) Heat map showing standard deviation of trapped particle position as a function of Pe and dimensionless system response time. The parameter values are: for calculating diffusion time: η = 0.0126 Pa-s, T = 298 K, d = 2.2 µm, Step = 4.95 µm; Controller gains: K_p = -20, K_i = -1.5, K_d = -1.4; a) τ_m varied from $1 \times 10^{-4} - 5 \times 10^{-3}$ with $\tau_v = 6.5 \times 10^{-5}$ (corresponding to 5 ms), b) τ_v varied from $1 \times 10^{-4} - 5 \times 10^{-3}$ with $\tau_m = 4.3 \times 10^{-4}$ (corresponding to 33 ms).

in particle fluctuations is observed. Thus, for small step change values, measurement delay becomes important only at high flow rates, and the particle trajectory is quite sensitive to large measurement delay values (standard deviation is ∼5 times the particle diameter).

2.4.2.3 Effect of system response times

The system response time represents the time over which the trap (e.g., microfluidic device, on-chip membrane value, tubing, pressure transducer) effectively responds to changes in the stagnation point upon receiving a signal from the LabVIEW program. In the simulation, the Péclet number Pe and the dimensionless system response time were varied, and the particle stability was determined while maintaining other parameters such as the measurement delay (set to 33 ms) and controller gains constant.

Fig. 2.8b shows a heat map illustrating trap stability (quantified as the standard deviation

of particle position) as a function of Pe and system response time . Particle fluctuations increase upon increasing Pe at a constant system response time. Analogously, particle fluctuations also increase upon increasing the system response time at a constant Pe. We also observe that larger Pe conditions require relatively smaller system response times to maintain the same degree of particle confinement compared to lower Pe. Increasing both Pe and the system response time results in an increase in the standard deviation of particle position, as shown in the upper right corner of Fig. 2.8b.

Fig. 2.9b shows a heat map of the dependence of particle standard deviation with the Péclet number and system response time, under experimental conditions. We note that the trend is similar to the high step change case, with fluctuations increasing with an increase in Péclet number and dimensionless system response time. Hence for large step changes, as long as the particle is stably trapped using a suitable measurement delay, we should reduce the valve response to get a tighter confinement (since the valve response has a greater effect on the particle oscillations). On the other hand, for small step changes, we see that measurement delay is critical and needs to be small in order to minimize oscillations.

2.5 Conclusions

The ability to trap and manipulate individual particles is a key technology for science and engineering. To this end, the hydrodynamic trap is a simple method that allows for precise confinement of micro- and nanoscale particles in free solution. In this work, we experimentally implemented and evaluated three different controllers - a proportional (P), a proportional-integral (PI), and a proportional-derivative (PD) - in order to gain an improved understanding of trap performance. We systematically investigated the effect of controller gain constants, system response times, and particle Péclet number on the stability of trapped particles.

Our results show that proportional and derivative controllers yield improvements in trap

stability, quantified by tightness of confinement or the magnitude of particle fluctuations about the set point, which tend to agree with previous simulations of a related microflow process [28]. On the other hand, integral control did not improve trap stability due to the nature of the process. Thus, P and PD control enhance the stability of the trapped particle in a microfluidic hydrodynamic trap because of the different time and length scales compared to the four-roll mill. In addition to experiments, we also developed a control model for simulating the response of the hydrodynamic trap, and we generally observed good agreement between experimental and simulation results. The control model allows for the system response and stability to be assessed over a wide range of the system parameters, including response times, measurement delay, and Péclet numbers.

Overall, our work provides an improved understanding of hydrodynamic trap stability as a function of control algorithms and system parameters, which will enable particle trapping under variable or uncertain experimental conditions (e.g., changing flow rates, solution viscosity, valve response or image acquisition rates). In addition, the implementation of more sophisticated control algorithms can be leveraged to stabilize particle trapping under challenging experimental conditions. Improved stability will broaden the range of applications for microfluidic-based trapping, which will enable the investigation of new physical phenomena currently inaccessible using alternative methods.

As the field of microfluidics continues to mature, increasingly advanced device designs will be required for on-chip assays, materials processing, and flow metering applications. Indeed, future generations of integrated microfluidic devices will employ automated feedback controllers for fluidics or pneumatic valves to achieve these goals [29, 30]. To this end, our work provides a solid framework for understanding the response of a microfluidic-based hydrodynamic trap to controller type and system parameters, which will be useful for guiding the design of next-generation, automated on-chip assays.

Chapter 3

Stokes trap for multiplexed particle manipulation[1]

In Chapter 2, we systematically investigated the effect of several controller parameters, and experimental parameters on the tightness of confinement of a single particle in the automated hydrodynamic trap. However, this setup is limited to trapping a single particle, and we wanted extend the capabilities of this setup to simultaneously manipulate several particles. In this chapter, we describe the Stokes trap, which is a new method for manipulation of multiple particles using the sole action of fluid flow. The Stokes trap relies on precise control over particle position in viscous-dominated (low Reynolds number) flows. Although prior work considered an open-loop algorithm for microfluidic assembly [31], this method was solely focused on computational studies of non-Brownian particles. Here, we develop and experimentally demonstrate a highly robust and scalable closed-loop control strategy that enables the precise manipulation of multiple particles and fluidic directed assembly of multiple particles.

3.1 Modeling and Design of the Stokes Trap

3.1.1 Fluidic model & governing equations

Consider the problem of manipulating P particles independently in a microfluidic device in which N channels intersect to form an N-sided polygonal flow device [31]. The objective is to control the two-dimensional center-of-mass position of each particle, which requires controlling $2P$ variables simultaneously. The control (or input) to this microfluidic system is the time-dependent flow rates within the N channels. Due to conservation of mass, however,

[1]This work was published in A. Shenoy, C.V. Rao, C.M. Schroeder, "Stokes trap for multiplexed particle manipulation and assembly using fluidics", *Proceedings of the National Academy of Sciences*, **113**, 3976-3981 (2016)

we can only prescribe $N-1$ flow rates independently because the net mass flow rate into the microdevice must be zero. In order to properly control multiple particles, we need at least as many control variables in the system as there are degrees of freedom, hence $N \geq 2P+1$. Therefore, a 4-channel microfluidic device can trap a single particle, which is consistent with prior work [16]. Nevertheless, the simple cross-slot design used in the (Generation 1) automated hydrodynamic trap does not have the required degrees of freedom for $P \geq 2$ particles.

We first consider the fluid dynamics within microfluidic device. At low Reynolds number (Stokes flow conditions), we can neglect fluid inertia which yields the following conservation equations [32]:

$$\nabla \cdot \mathbf{v} = 0, \qquad -\nabla p + \mu \nabla^2 \mathbf{v} + \rho \mathbf{b} = 0 \tag{3.1}$$

where $\mathbf{v}$ is fluid velocity, p is pressure, μ is viscosity, ρ is density and $\mathbf{b}$ is a volumetric (body) force. In typical microfluidic devices, the vertical channel height H is much smaller than channel width W such that $H < W$. The velocity profile is parabolic in the vertical direction, with the height-averaged velocity being proportional to the gradient of pressure. Using the formalism of a Hele-Shaw flow cell [32], each inlet channel is approximated as a 2-D hemispherical point source, and the height-averaged fluid velocity inside the cross-slot is expressed as a linear superposition of N source flows [31]:

$$\mathbf{v}(\mathbf{x}) = \frac{1}{\pi H} \sum_{i=1}^{N} \frac{(\mathbf{x} - \mathbf{R}_i)}{\|\mathbf{x} - \mathbf{R}_i\|^2} q_i \tag{3.2}$$

where $\mathbf{R}_i \in \mathbb{R}^2$ is the position vector of the point source corresponding to the i^{th} channel and $\mathbf{q} \in \mathbb{R}^N$ is a vector containing flow rates whose i^{th} element is the flow rate through the i^{th} channel. Of course, the choice of q_i must satisfy mass conservation such that:

$$\sum_{i=1}^{N} q_i = 0 \tag{3.3}$$

where flow into the cross-slot is defined to be positive ($q > 0$). We validated the point source model by determining the velocity field inside a 3-D microfluidic polygonal geometry using computational fluid dynamics (COMSOL). The height-averaged fluid velocity was compared to our model (Eq. (3.2)) as a function of position inside the microdevice (Section 3.2.1.2). In general, we found that this model accurately captures the fluid flow profiles in the device (to within $\sim$2%), and minor deviations can be reduced by suitable choice of the aspect ratio of the channels.

Using this model, the fluid velocity at a point inside the polygonal device is completely determined by the imposed flow rates q_i. Let us assume that a particle is advected with the same local velocity as the fluid, such that the particle's center-of-mass velocity is given by Eq. (3.2). It is then possible to invert Eq. (3.2) and Eq. (3.3) to obtain the flow rates q_i required to achieve a set of desired particle velocities. Let the instantaneous position of the particle be $\mathbf{x} \triangleq [x, y]^T \in \mathbb{R}^2$. The governing equations for the particle are:

$$\frac{d\mathbf{x}}{dt} = \mathbf{F}(\mathbf{x}, \mathbf{q}, \mathbf{R}) \triangleq \frac{1}{\pi H} \sum_{i=1}^{N} \frac{(\mathbf{x} - \mathbf{R}_i)}{\|\mathbf{x} - \mathbf{R}_i\|^2} q_i \tag{3.4a}$$

$$\sum_{i=1}^{N} q_i = 0 \tag{3.4b}$$

Although it is possible to completely determine the set of flow rates q_i via matrix inversion, this method is generally not practical for experiments due to unreasonably large fluxes required for certain scenarios such as close approach of two particles. In order to circumvent this issue, we utilize a control algorithm for determining q_i.

3.1.2 Model predictive control

Given the governing equations for fluid flow, the next challenge lies in implementing a control algorithm to determine experimentally feasible flow rates q_i to manipulate particles. In a recent computational study on particle assembly [31], the flow rates required for maneuvering particles were obtained by minimizing an objective function using Pontryagin's

maximum principle. However, this approach assumes that particles are non-Brownian and therefore move deterministically with the flow; moreover, this approach does not consider perturbations in flow rates or modeling inaccuracies that may arise naturally in experiments.

Steering a single particle from an initial position $\mathbf{x}^0$ to the final position $\mathbf{x}^F$ requires imposed flow rates that vary with time and involves several experimental challenges. First, we aim to confine and manipulate Brownian particles (< 10 µm in diameter) for which thermal fluctuations are significant, thereby yielding stochastic, non-deterministic particle trajectories. Second, it is possible that the fluidic model described by Eq. (3.2) may differ from the actual experimental flow field due to modeling inaccuracies and/or actuator resolution limits, which necessitates the use of a robust control algorithm. Third, we found that solution of adjoint equations was computationally intensive and not well suited for real-time experimental implementation. In our work, we aim to solve the system equations on the millisecond timescale at typical acquisition rates of 30 Hz, which necessitates a robust control strategy that can rapidly solve the governing equations. For these reasons, we implement a model predictive control (MPC) algorithm for precise control [33].

We briefly discuss the model predictive control (MPC) strategy followed by experimental implementation. First, a finite time horizon $[0, T]$ is selected and divided into a discrete number of intervals M of equal size, such that each interval is equal to the sampling time. The imposed flow rates are assumed to be piecewise constant during each interval but change from one interval to the next. Next, a matrix of flow rate vectors is defined for each interval in the time horizon such that $\mathbf{Q} = [\mathbf{q}^1, \mathbf{q}^2, \ldots, \mathbf{q}^M]$. Given a certain combination of flow rates over the horizon and the current position $\mathbf{x}^0$, we can calculate the trajectory of the particle over the time horizon by numerically solving Eq. (3.2). We discretize the trajectory at the endpoints of each interval, denoting the position of the particle at these points as $\mathbf{X} = [\mathbf{x}^0, \mathbf{x}^1, \ldots, \mathbf{x}^M]$. We also define an integrator variable $\mathbf{e}$, such that $d\mathbf{e}/dt = \mathbf{x} - \mathbf{x}^F$, with a corresponding matrix $\mathbf{E} = [\mathbf{e}^0, \mathbf{e}^1, \ldots, \mathbf{e}^{M-1}]$.

We seek to determine particle trajectories that minimize distance traveled while also

minimizing flow rates, where the latter condition ensures that the flow rates have physically realizable values in experiments and that the optimization problem is well posed. However, not all trajectories from the initial position $\mathbf{x}^0$ to the final positions $\mathbf{x}^F$ are feasible or desirable, because some trajectories might violate mass conservation or take a circuitous path. To systematically obtain optimal trajectories and flow rates, $\mathbf{Q}$ is expressed as the argument of an optimization problem:

$$\begin{aligned}
\min_{\mathbf{X},\mathbf{E},\mathbf{Q}} \quad & J = \sum_{k=0}^{M-1} \left\{ \alpha \left(\|\mathbf{x}^k - \mathbf{x}^F\|^2 \right) + \beta \|\mathbf{q}^k\|^2 + \delta \|\mathbf{e}^k\|^2 \right\} \\
& + \gamma \left(\|\mathbf{x}^M - \mathbf{x}^F\|^2 \right) && \text{(3.5a)} \\
\text{s.t.} \quad & \frac{d\mathbf{x}}{dt} = \mathbf{F}(\mathbf{x}, \mathbf{q}, \mathbf{R}), \quad \mathbf{x}(0) = \mathbf{x}^0 && \text{(3.5b)} \\
& \frac{d\mathbf{e}}{dt} = \mathbf{x} - \mathbf{x}^F && \text{(3.5c)} \\
& \sum_{i=1}^{N} q_i = 0 && \text{(3.5d)}
\end{aligned}$$

where J is the objective function and α, β, γ and δ are scalar weights that can be dynamically tuned to obtain the desired response, for example, removing the offset between the desired target position and the current position.

By solving the optimization problem, we obtain flow rates $\mathbf{Q}$ that move a particle from its current position to a target position at a minimal cost as determined by the weighting factors. However, in our approach, we only apply the first set of flow rates $\mathbf{q}^1$ from the calculated $\mathbf{Q}$, and then we remeasure the $\mathbf{x}^0$ after one sampling period (*i.e.* T/M seconds) which becomes the initial condition for the optimization problem at the next sampling instant. In this way, flow rates are calculated for the entire trajectory over the horizon, but only the flow rates for the first interval are applied, at which point the particle position is remeasured. This process is repeated continuously throughout the experimental period. The MPC strategy is highly tolerant to fluctuations and experimental perturbations described above.

An additional advantage of formulating the trapping process as an optimization problem

is that scaling the platform to trap multiple particles ($P > 1$) requires only simple modifications to the model. To trap 2 particles, we choose a 6-channel cross-slot geometry and redefine the state vector $\mathbf{x} \triangleq [\mathbf{x}_1^T, \mathbf{x}_2^T]^T$. The new optimization problem is thus written as:

$$\begin{aligned}
\min_{\mathbf{X},\mathbf{E},\mathbf{Q}} \quad & J = \sum_{k=0}^{M-1} \left\{ \alpha \left(\|\mathbf{x}^k - \mathbf{x}^F\|^2 \right) + \beta \|\mathbf{q}^k\|^2 + \delta \|\mathbf{e}^k\|^2 \right\} \\
& + \gamma \left(\|\mathbf{x}^M - \mathbf{x}^F\|^2 \right) && \text{(3.6a)} \\
\text{s.t.} \quad & \frac{d\mathbf{x}}{dt} = [\mathbf{F}^T(\mathbf{x}_1, \mathbf{q}, \mathbf{R}), \mathbf{F}^T(\mathbf{x}_2, \mathbf{q}, \mathbf{R})]^T, \quad \mathbf{x}(0) = \mathbf{x}^0 && \text{(3.6b)} \\
& \frac{d\mathbf{e}}{dt} = \mathbf{x} - \mathbf{x}^F && \text{(3.6c)} \\
& \sum_{i=1}^{N} q_i = 0 && \text{(3.6d)}
\end{aligned}$$

3.1.3 Experimental implementation using ACADO

The governing equations of motion are nonlinear and the optimization problem is constrained. Thus, conventional solution techniques are too slow to achieve robust control at typical camera acquisition rates of 30 Hz. For example, we found that MATLAB requires ∼15 minutes to solve an optimization problem in which 2.2 µm diameter Brownian particles are moved over a distance of ∼30 µm. To overcome this issue, we employ the ACADO (Automatic Control and Dynamic Optimization) toolkit [34–36], which enables microsecond solutions of constrained nonlinear MPC problems via code generation. In a typical experiment, we found that the solution process was completed in ∼500 µs using ACADO, which is significantly faster than our feedback time of 33 ms.

3.2 Methods & Materials

3.2.1 Device design and fabrication

The overall designs for the 4-channel and 6-channel microfluidic devices are shown in Fig. 3.1a,b. For calculating the locations of the N point sources $\mathbf{R}_i$, we can either use the inscribed circle or the circumcircle of the N-sided polygon, as illustrated in Fig. 3.1c,d. For a 4-channel cross-slot we use the inscribed circle and for the 6-channel cross-slot we use the circumcircle. The width of the channel is $W = 400$ µm. Eq. (3.7) describes the

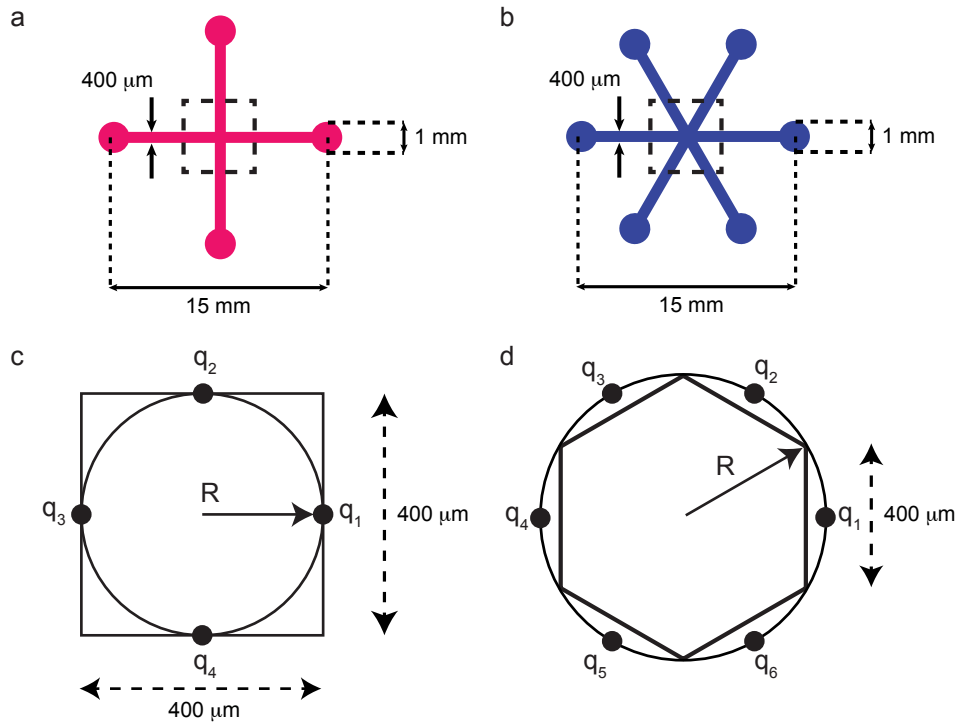

Figure 3.1: Device design for the single particle and two particle trap.

relationship between the radius of the inscribed circle and the width of the channel, while Eq. (3.8) describes the relationship between the radius of the circumcircle and the width of the channel. After defining the radius using one of the two methods above, in all cases the

coordinates $\mathbf{R}_i$ of the i^{th} point source are given by Eq. (3.9):

$$R = \frac{W}{2}\cot\left(\frac{\pi}{N}\right) \tag{3.7}$$

$$R = \frac{W}{2\sin\left(\frac{\pi}{N}\right)} \tag{3.8}$$

$$\mathbf{R}_i = R\left[\cos\left(\frac{2(i-1)\pi}{N}\right), \sin\left(\frac{2(i-1)\pi}{N}\right)\right]^T \tag{3.9}$$

3.2.1.1 Microfluidic device fabrication

Standard procedures for PDMS-based soft lithography were followed to fabricate 4 and 6 channel microdevices. A mold was first prepared by spin-coating a thin layer (∼100 µm) of negative photoresist (SU-8 2050) onto a 3" diameter silicon wafer, followed by UV exposure using a high-resolution transparency film as a mask. Molds were then developed using propylene glycol methyl ether acetate (PGMEA). For replica molding, these layers were treated with trichloro (1H, 1H, 2H, 2H-perfluorooctyl) silane vapor to facilitate straightforward removal of the PDMS layer in the subsequent step. Next, PDMS with a 10:1 (w/w) base:crosslinker ratio was poured onto the mold and baked overnight at 65° C. This slab was then peeled off the mold, and access holes are punched to the channels using a needle with a blunt tip. Finally, the PDMS slab was bonded to a glass coverslip using plasma oxidation to obtain a functional device.

3.2.1.2 COMSOL Simulations

To validate the accuracy of the Hele-Shaw equation (Eq. (3.2)), we simulated the full 3-D flow field inside a hexagonal cross-slot using COMSOL. A 3-D cross-slot was constructed in COMSOL, with the center of the hexagonal flow chamber at the origin, and the height of the device oriented along the positive z-direction. We parameterized the geometry of the device in terms of the width W and height H of the channels. In all cases, we impose a value of $q = 40$ μL/hr for channels corresponding to q_1 through q_5, and a value of $q = 200$

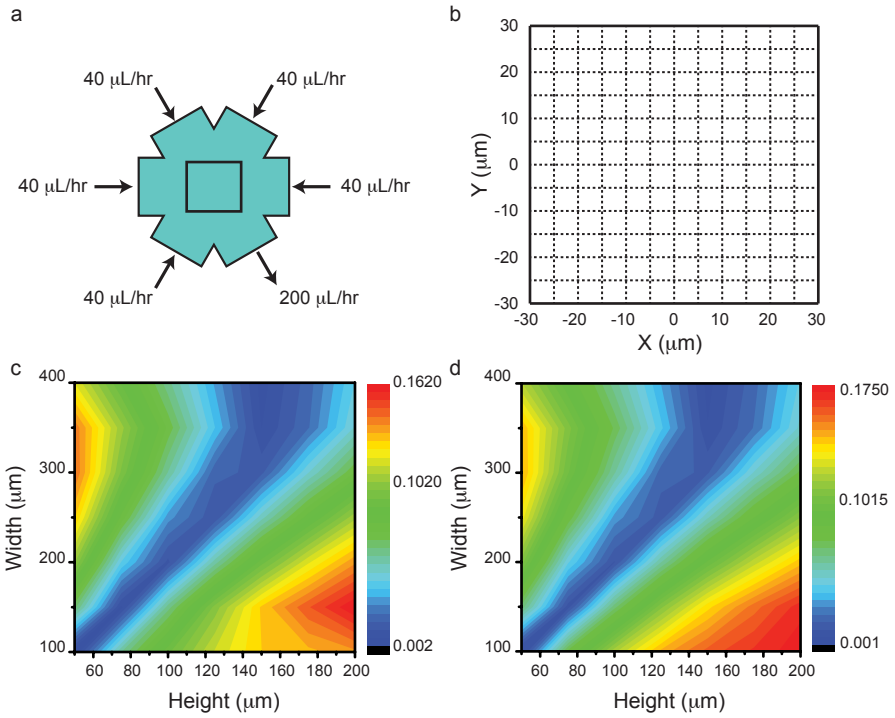

Figure 3.2: COMSOL simulations to validate flow models. (a) Schematic of the 6-channel cross-slot with the imposed flow rates. The square at the center of the cross-slot represents the grid from which velocity information is obtained. (b) An $x - y$ section of the 3-D rectangular grid for obtaining velocity information. (c) Mean relative error $\langle e_{u_x} \rangle$ in the x component of the height averaged velocity. (d) Mean relative error $\left\langle e_{u_y} \right\rangle$ in the y component of the height averaged velocity.

μL/hr for q_6 (Fig. 3.2a). These flow rates were chosen so that the net mass flow rate into the cross-slot is zero. In the COMSOL model, we specify the no-slip boundary condition on all internal surfaces, and prescribe the flow rates mentioned above on the channel cross-sections. This model is then solved using the Stokes equations in COMSOL. The entire geometry is meshed using a "physics-defined" sequence and a "normal" mesh size, which effectively results in a maximum element size of 39 µm and a minimum element size of 12 µm based on the geometry. For the flow simulations, the channel height was varied between 50 and 200 µm (the height was stepped by 25 µm), whereas the channel width was varied between 100 and 400 µm (the width was stepped by 50 µm).

Following this step, we define a 3-D grid consisting of $13 \times 13 \times 11$ points inside the

cross-slot geometry. In the x and y directions, the grid consists of 13 regularly spaced points spanning -30 µm to 30 µm, whereas in the z direction, we choose 11 regularly spaced points spanning 0 to H. An x, y section of this grid has been shown in Fig. 3.2b. For every combination of W and H, we record the 3-D velocity information at the gridpoints, and then calculate the height averaged velocity at the gridpoints shown in Fig. 3.2b. After this, we calculate the absolute mean relative error in the x and y components of the height-averaged velocity from COMSOL and the predicted velocity from the Hele-Shaw equation using the following equations:

$$\langle e_{u_x} \rangle = \left| \frac{1}{K} \sum_{1}^{K} \frac{u_{x,HS} - u_{x,COMSOL}}{u_{x,COMSOL}} \right| \tag{3.10}$$

$$\left\langle e_{u_y} \right\rangle = \left| \frac{1}{K} \sum_{1}^{K} \frac{u_{y,HS} - u_{y,COMSOL}}{u_{y,COMSOL}} \right| \tag{3.11}$$

Here $u_{x,HS}$ and $u_{y,HS}$ are the x and y components of the velocity from the Hele-Shaw equation, respectively, $u_{x,COMSOL}$ and $u_{y,COMSOL}$ are the velocities obtained from COMSOL, and K is the total number of points in the 2-D grid (Fig. 3.2b). In this way, $\langle e_{u_x} \rangle$ and $\left\langle e_{u_y} \right\rangle$ are the mean relative error in the x and y components of the height-averaged velocity. These quantities were calculated for all combinations of W and H that we explored in the COMSOL simulations. From Fig. 3.2c,d, we see that by selecting the aspect ratio suitably, we obtain an accurate description of the flow field, with an error of approximately 2%.

3.2.1.3 Mesh refinement study

We validated the COMSOL simulation results by performing a series of simulations with different (and smaller) mesh element sizes. Here, we repeated the simulations with a refined mesh in which the maximum element size was set to 20 µm and the minimum element size was set to 5 µm. We summarize the values obtained from the original mesh and the refined mesh in Table Table 3.1. In general, reducing the mesh size produces only minor changes in the error values.

	Max Element Size: 39 μm				Max Element Size: 20 μm			
	Height (μm)				Height (μm)			
Width (μm)	50	100	150	200	50	100	150	200
100	0.21%	9.09%	12.69%	13.56%	0.16%	9.14%	12.72%	14.18%
150	6.39%	5.95%	12.80%	16.22%	6.38%	6.13%	13.09%	16.61%
200	10.26%	1.04%	8.99%	13.61%	10.29%	1.23%	9.23%	14.16%
250	12.75%	2.92%	4.99%	10.54%	12.71%	2.77%	5.31%	10.94%
300	14.22%	5.67%	1.55%	7.20%	14.23%	5.55%	1.93%	7.71%
350	14.07%	7.05%	0.70%	4.78%	14.09%	6.85%	0.33%	5.17%
400	11.67%	5.89%	0.50%	4.23%	11.68%	5.69%	0.26%	4.51%

(a) Mean relative error $\langle e_{u_x} \rangle$ in the x component of the height averaged velocity.

	Max Element Size: 39 μm				Max Element Size: 20 μm			
	Height (μm)				Height (μm)			
Width (μm)	50	100	150	200	50	100	150	200
100	0.20%	11.50%	15.85%	17.50%	0.22%	11.60%	16.15%	17.98%
150	6.51%	6.43%	13.45%	16.96%	6.52%	6.58%	13.75%	17.39%
200	10.43%	1.11%	9.25%	13.94%	10.46%	1.22%	9.50%	14.49%
250	12.93%	2.94%	5.05%	10.65%	12.94%	2.77%	5.41%	11.09%
300	14.30%	5.71%	1.56%	7.31%	14.30%	5.57%	1.96%	7.80%
350	14.12%	7.04%	0.69%	4.83%	14.15%	6.87%	0.32%	5.21%
400	11.70%	5.88%	0.49%	4.26%	11.69%	5.75%	0.28%	4.56%

(b) Mean relative error $\langle e_{u_y} \rangle$ in the y component of the height averaged velocity.

Table 3.1: Comparison of the results from the "physics-defined" mesh yielding a maximum mesh size of 39 µm and the finer refined mesh with maximum size of 20 µm.

3.2.2 Scaling and non-dimensionalization

The optimization problem (Eq. (3.5) and Eq. (3.6)) is solved numerically in real-time during experiments, and it is important to scale all quantities to be $O(1)$. We define a characteristic timescale t_c as the time required to replace the volume of fluid inside the flow chamber at a characteristic flow rate q_c such that $t_c = \pi R^2 H/q_c$, where H is the channel height and $R = \sqrt{3}W/2$ is the radius of the circle inscribed inside the hexagonal fluid chamber, where W is the inlet channel width. We define a characteristic flow rate $q_c = 0.5$ μL/hr and a characteristic length scale $l_c = R$. These definitions yield a characteristic velocity of $v_c = R/t_c$. All controller equations are scaled using these variables, such that Eq. (3.4) becomes

$$\overline{\mathbf{v}} = \sum_{i=1}^{N} \frac{(\overline{\mathbf{x}} - \overline{\mathbf{R}}_i)\overline{q_i}}{\|\overline{\mathbf{x}} - \overline{\mathbf{R}}_i\|^2}$$

The dimensionless controller equations are solved using ACADO. We used a custom LabVIEW program for processing images acquired by the CCD camera in order to localize particles. The LabVIEW program communicates particle locations with ACADO using a standard TCP socket. After determining optimal trajectories, ACADO transmits flow rates back to LabVIEW, which then converts flow rate values to pressures and appropriately actuates the pressure regulators using analog output using an analog output card (NI PCI-6713) and connector block (NI BNC 2110).

3.2.3 Optimization parameters

Typical values for the weights in the objective function are: $\alpha = 1$, $\beta = 10^{-5}$, $\gamma = 1$ and $\delta = 10$. Of course, these values can be tuned dynamically throughout any experiment. In the following, we describe the rationale behind assigning the values of the weights in the controller. In all experiments, we trap a particle by minimizing the objective function, subject to certain constraints (Eq. 3.6). Here, we define the "target position" as the final

position $\mathbf{x}^F$. In the objective function, α represents the penalty on a trajectory that deviates from the target position $\mathbf{x}^F$, β represents the penalty for using high values of flow rates, δ penalizes high values of integrated error, and γ penalizes the error between the predicted position at the end of the horizon and the target position. A custom LabVIEW program allows the user to change these weights continuously during the experiment. Initially, we studied the system response in the absence of an integrator ($\delta = 0$). Here, we first set the weights α, β and γ to 1 (in other words, equally weight all terms). However, this generally results in ineffective trapping of characteristic micron-sized particles, because the calculated controls are too weak. Thus, in order to increase the magnitude of the applied controls, we reduced the value of the parameter β. However, if we set a very low value of β, then there is a possibility of obtaining an optimization problem that does not have a feasible solution. Eventually, through trial and error parameter tuning, we found that $\beta = 10^{-5}$ works well for particle trapping. However, we then observed an offset between the equilibrium position of the particle and the target location. To fix this issue, we introduced an integrator term into the controller, and we initially set the weight δ to 1. In order to remove the offset, we needed to reduce the error (and consequently the integrated error), which is accomplished by increasing δ. Again, we found that $\delta = 10$ resulted in stable trapping for the experiments described in this chapter. We note that the values of the weights are dependent on the particular manner in which variables are scaled (using dimensionless groups and characteristic scales), as discussed in the Section 3.2.2.

3.2.4 Experimental setup and sample preparation

The microfluidic device was mounted on the stage of an inverted microscope (Olympus IX71) equipped with a 10x objective lens and a CCD camera (AVT Stingray F-033B / Point Grey GS3). The inlet/outlet channels on the microdevice were connected to fluidic reservoirs (Elveflow, France) through FEP tubing (IDEX Health & Science), and the reservoirs were pressurized using electronic pressure regulators (Proportion Air). In all experiments, the

buffer is a glycerol-water solution with a viscosity of 12.6 Pa-s at room temperature (25 ^{o}C). For trapping experiments, we used 2.2 µm diameter fluorescent polystyrene beads (Nile Red, Spherotech Inc). For assembly experiments, we used 10.6 µm and 7.4 µm diameter polystyrene beads coated with streptavidin and biotin (Spherotech and Bangs Laboratories, respectively).

3.2.4.1 Flow rates to pressure conversion

For converting the flow rates into pressure values, we recast the microfluidic device into an effective circuit, as shown in Fig. 3.3. We assume that the cross-slot has an average pressure P_0. Thus, the pressure P_i that must be imposed on the i^{th} fluid reservoir can be determined using:

$$P_i = P_0 + q_i Z_i \tag{3.12}$$

where Z_i is the hydrodynamic resistance of the fluidic path between the reservoir and the cross-slot, which includes the fluidic reservoir, FEP tubing, and the channel itself. Here, q_i is the flow rate value obtained from ACADO. In our experiments, we typically set P_0=13.8 kPa (2 Psi), and Z_i=5×10^{15} Pa-s/m^3 (all channels are assumed to have the same hydrodynamic resistance). Using Eq. (3.12), we determine the pressures to be imposed on all fluid reservoirs. In this way, the entire setup operates at a positive pressure, which allows any channel to behave as an inlet/outlet.

3.3 Results

3.3.1 Stokes Trap: Overview and design

A schematic illustration of the 4- and 6-channel microdevices is shown in Fig. 3.4a. In these experiments, we use a 4-channel device for trapping a single particle and a 6-channel device for trapping two particles. For trapping two particles, we found that an

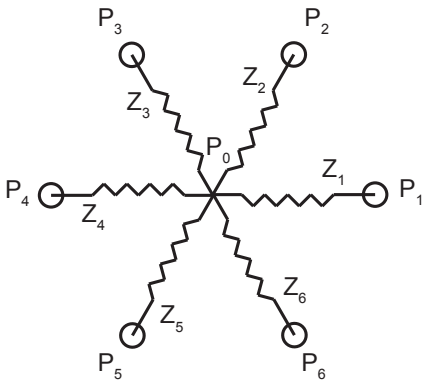

Figure 3.3: Fluidic circuit

additional control variable ($N = 6$) provides more flexible control, even though the system has $2P + 1 = 5$ degrees of freedom in this case. Fig. 3.4b shows a schematic of the overall experimental setup for the Stokes trap. The setup consists of 6 pressure regulators that control fluid flow by pressurizing 6 distinct fluid reservoirs, which are in turn connected to a microfluidic device mounted on the stage of an inverted microscope. The Stokes trap operates at a net positive pressure such that each fluidic channel can function as an inlet or outlet channel with net positive or net negative flux, respectively, by simply varying pressure (Section 3.2.4.1). A schematic block diagram showing implementation of the control loop is shown in Fig. 3.4c. The algorithm begins when a CCD camera acquires a snapshot and relays the image to a custom LabVIEW program. Next, LabVIEW localizes particles and determines the 2D center-of-mass coordinates of target particle(s). The LabVIEW program allows the user to dynamically set the target setpoint positions for both particles through a graphical user interface (GUI). Next, the particles' coordinates are transmitted to the ACADO controller to determine the requisite flow rates for steering them to the desired positions. In this step, the controller solves Eq. (3.6) to obtain the set of flow rates q_i for each channel and transmits the information back to LabVIEW. Finally, LabVIEW converts these flow rates to corresponding pressures and actuates the pressure regulators, which deliver the required flow rates to the device via the fluid reservoirs.

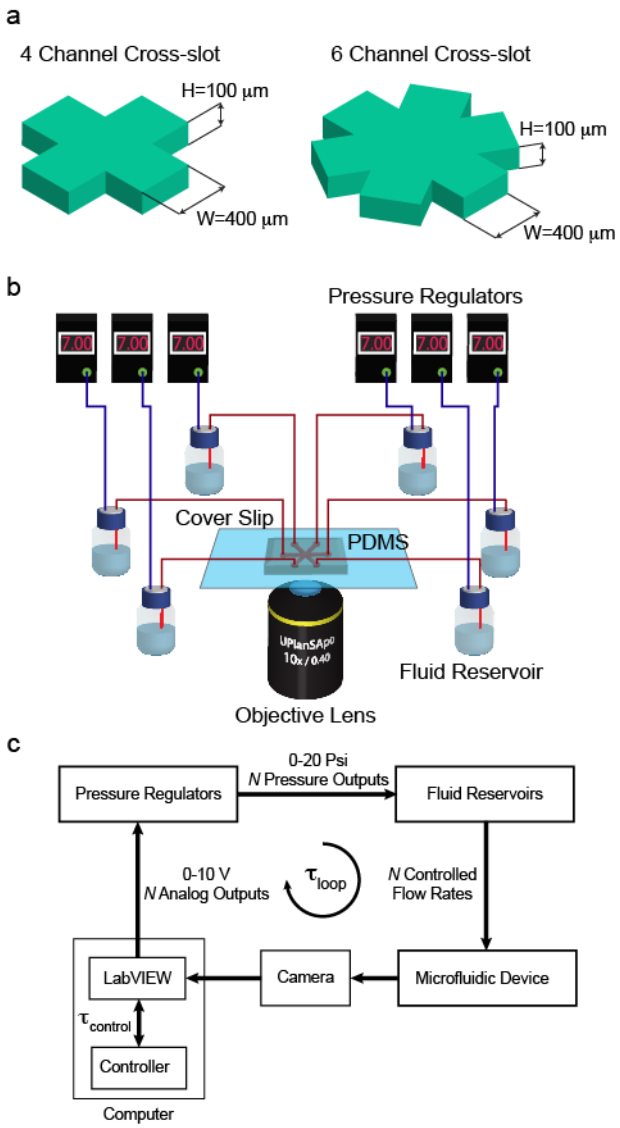

Figure 3.4: Overview of the Stokes trap and control algorithm. (a) Schematics of 4-channel and 6-channel microfluidic devices for manipulating 1 and 2 particles, respectively. (b) Overview of the experimental setup. Inlet/outlet channels in the microfluidic device are connected to fluidic reservoirs that are pressurized by regulators controlled by a custom LabVIEW program. In this way, the fluidic reservoirs drive fluid flow in the microdevice. (c) Block diagram of the control loop for particle manipulation and trapping, with typical time constants of $\tau_{loop} = 33$ ms and $\tau_{control} = 500$ µs.

3.3.2 Fluidic model & streamline topologies

Before embarking on particle trapping, we first validated the fluidic model (Eq. (3.2)) by experimentally determining streamline topologies using particle tracking and fluorescence microscopy. In these experiments, we use an aqueous glycerol buffer (pH 8.0, viscosity $\eta =$ 12.6 cP) containing 2.2 µm diameter fluorescent beads to characterize the flow field. We use standard bead tracking algorithms (ImageJ with MOSAIC plugin [37]) to determine bead trajectories over at least 30 s durations, which is suitable for quantitative flow field analysis at typical strain rates of 1-10 s^{-1}. Fig. 3.5a,b illustrate the direction and magnitude of the imposed flow rates in the 6-channel device during these experiments. Experimental streamline topologies are plotted in Fig. 3.5c,d. Interestingly, we observe two distinct flow topologies which we refer to as 'linked arms' (Fig. 3.5c) and 'non-linked arms' topologies (Fig. 3.5d). In both cases, we clearly observe the existence of two stagnation points, which facilitates the independent trapping of two particles. In the linked arms topology, we observe that the principal axis of extension for the right stagnation point corresponds to the principal axis of compression for the left stagnation point. In the non-linked arms topology, the stagnation points are no longer connected by streamlines. We obtained similar streamline topologies by numerically solving Eq. (3.2), as shown in Fig. 3.5e,f.

3.3.3 Trapping single particles using the Stokes trap

We first characterized the performance of the Stokes trap by confining single particles at a target position and determining the trap stiffness. The Stokes trap can be used to confine particles in either quiescent conditions (*i.e.* no net flow if the particle is at the target position) or in net flow conditions (*i.e.* net flow even if the particle is at target position). In quiescent conditions, fluid flow is only applied to correct for Brownian motion of the particle, and in this case, the Stokes trap functions in an analogous fashion to electrokinetic traps [9]. As an aside, we note that unlike the Stokes trap, the Generation 1 automated hydrodynamic trap cannot operate under quiescent conditions. The Generation 1 trap uses an on-chip

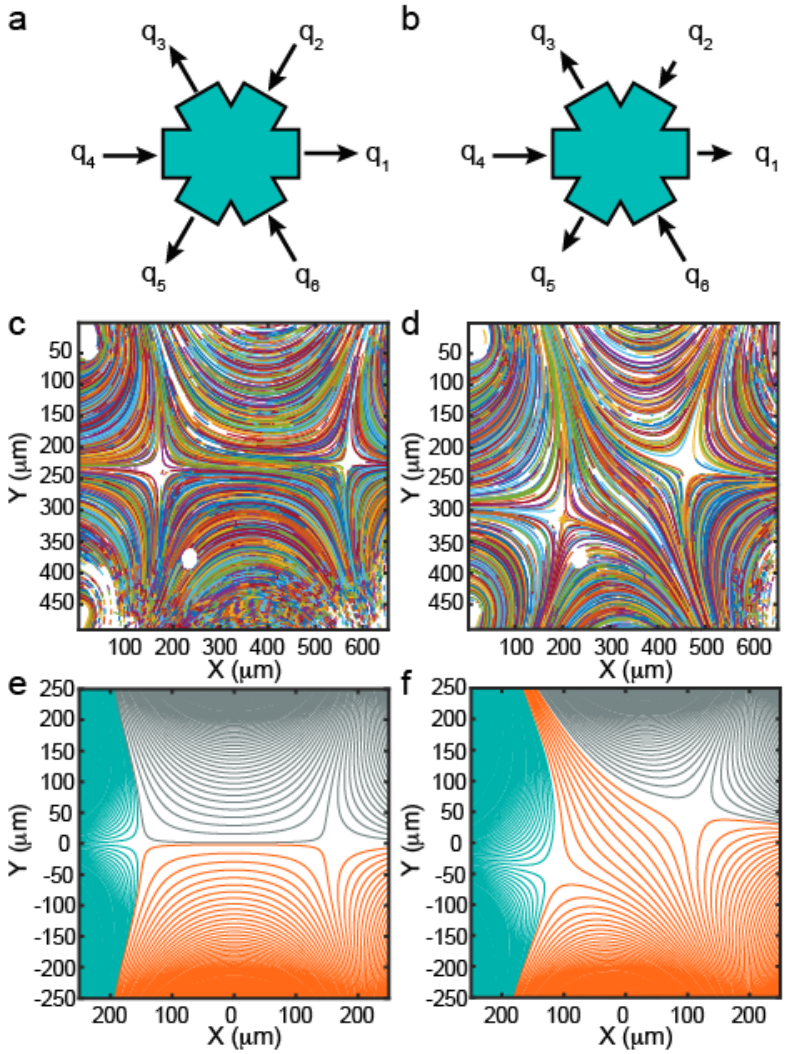

Figure 3.5: Streamline topologies in a 6-channel microdevice from experiments and computation. (a)-(b) Schematic of the relative magnitude and direction of the flow rates for generating the streamline topologies in the figures below. Arrows pointing inwards represent flow entering the device, and arrows pointing outwards represent flow exiting the device. The size of the arrows signifies the relative magnitude of the flow rates. (c) Experimental streamlines showing the 'linked-arms' topology, generated when the flow rates have a specific symmetry. Two stagnation points are clearly visible. (d) Experimental streamlines showing the 'non-linked arms' topology, generated if the symmetry in (c) is broken. (e)-(f) Streamline topologies obtained from numerical solution of Eq. (3.2). For display, streamlines emanating from inlet channels are plotted using distinct colors.

membrane valve to control flow, and the membrane valve is incapable of influencing particle position in the absence of a net imposed flow.

In order to quantify trap performance, we used the Stokes trap with MPC (Eq. (3.5)) to confine a single (2.2 µm diameter) fluorescent bead in a 4-channel device, and we recorded the particle trajectory for a duration of 400 s (Fig. 3.6a). We use a bead tracking algorithm to localize particle position, followed by determination of the power spectral density (PSD) of the particle position fluctuations (Fig. 3.6b). We fit the PSD with a Lorentzian and a Maximum Likelihood estimator [38, 39], and the corner frequency f_c was determined to be 0.64 Hz and 0.82 Hz using these methods, respectively. We determined the trap stiffness $\kappa = 2\pi\zeta f_c$ as 1.1×10^{-3} pN/nm and 1.4×10^{-3} pN/nm, where ζ is the Stokes drag of the bead. These trapping stiffnesses are comparable to a weak optical trap [40]. Moreover, we found that the MPC algorithm and the overall design of the Stokes trap yields a tighter trap (∼5-7x increase in trap stiffness) compared to the previous Generation 1 automated hydrodynamic trap, which only used a simple proportional controller and an on-chip valve to yield a stiffness of 2.0×10^{-4} pN/nm under similar experimental conditions [14].

3.3.4 Manipulating two particles using the Stokes trap

We next used the Stokes trap to confine and manipulate two particles simultaneously (Fig. 3.7). Here, we used a 6-channel microfluidic device to manipulate two 2.2 µm diameter particles in an arbitrary scenario. First, the two particles are trapped approximately 198 µm apart. Next, the target positions of both particles are instantaneously interchanged, and the MPC given by Eq. (3.6) is used to control the process of particle interchange. In this experiment, we do not prescribe the intermediate trajectory for either particle, rather, the trajectory is generated by the controller. We found that the controller successfully generates smooth trajectories in real time by minimizing the objective function, as shown in Fig. 3.7. Using this strategy, the particle position interchange occurs over a relatively short timescale, with the entire process completing in 22.5 s.

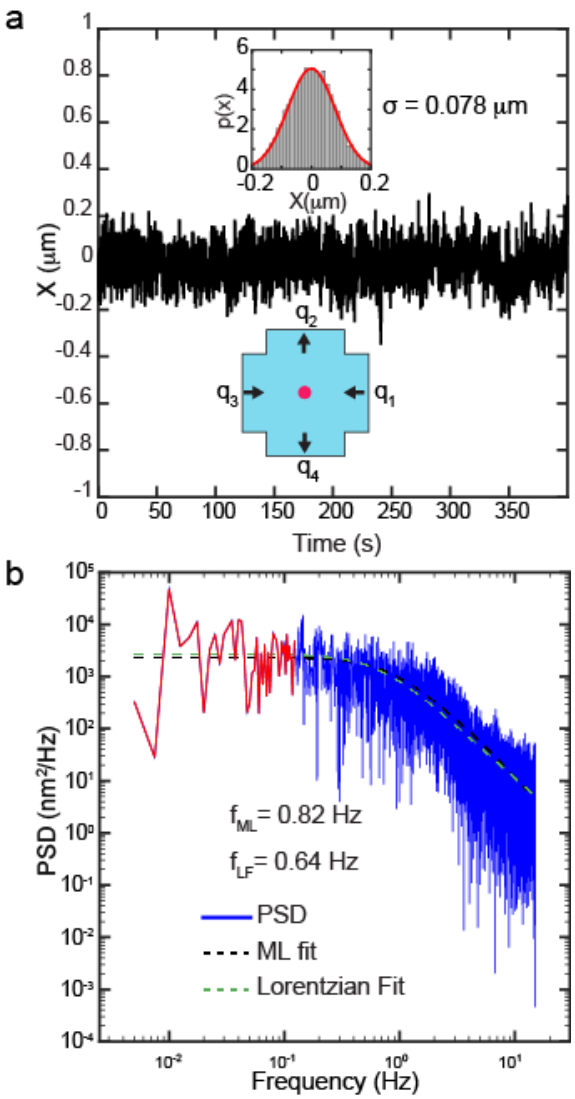

Figure 3.6: Characterizing the performance of the Stokes trap. (a) Trajectory of trapped 2.2 μm diameter bead over a period of 400 s. (Inset, top) Probability distribution of the position of the particle. (Inset, bottom) Schematic of microdevice used for trapping. (b) Power spectral density (PSD) particle position flucutations for the trajectory shown in part (a). The PSD is analyzed to determine the corner frequency f_c.

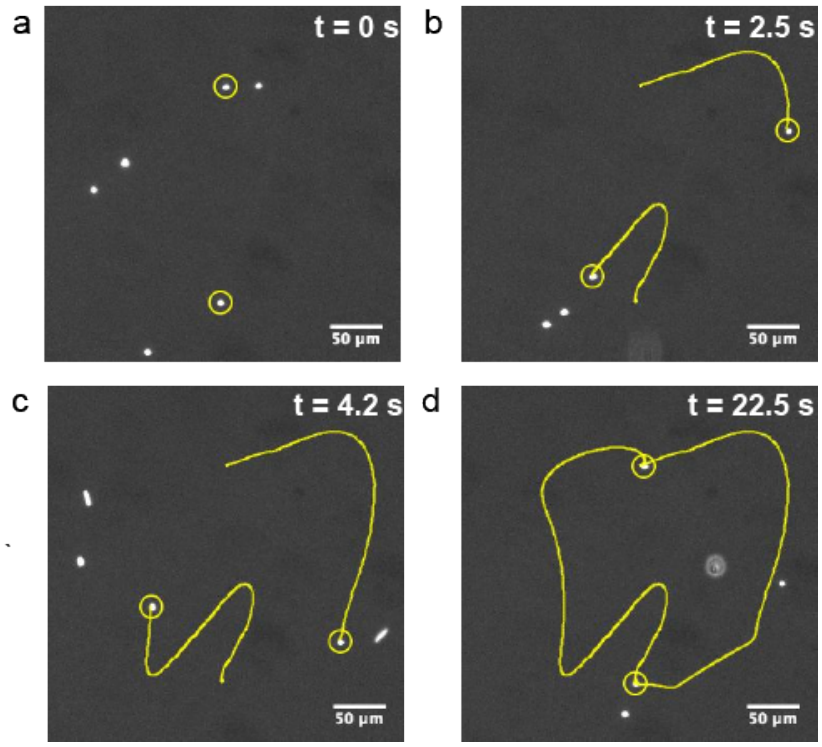

Figure 3.7: Manipulating two particles using the Stokes trap, where the objective is to switch the center-of-mass positions of both particles. (a) At time $t = 0$ s, two 2.2 µm diameter fluorescent beads are initially trapped ∼198 µm apart. At t=0.033 s, we instantaneously interchange the target positions of both particles, after which the controller generates a trajectory for each particle and calculates and applies the flow rates. (b)-(c) Tracing the two particle trajectories during the experiment, with the yellow line showing the past history of both particles. (d) The process finishes at $t = 22.5$ s, at which time the particle positions have been interchanged.

We further demonstrate the precise manipulation of two particles along pre-programmed paths (Fig. 3.8). The experiment begins by tracking two freely-suspended particles in the field of view, and at time $t = 0$ s, the controller is activated. First, the controller traps both particles, and the two particles are smoothly delivered to their respective (initial) target positions. Next, the target position is slowly and repeatedly stepped along a pre-programmed path, during which time the controller works to continuously move the particles synchronously with the target position. In this experiment, the target positions are programmed to trace the letter 'I', and the process completes after 328 s. As shown in Fig. 3.8a-d, we are able to accurately and precisely control both particles along a predetermined path that spans hundreds of microns, which is orders of magnitude larger than the particle size. For each experiment, we also record the flow rates required for particle manipulation. Fig. 3.8e shows the flow rates during the two particle manipulation experiment.

3.3.5 Fluidic-directed assembly of particles

We also used the Stokes trap to assemble two small particles in solution (Fig. 3.9). In this experiment, the goal is to link two 'sticky' particles together via directed assembly, in particular by linking a 7.4 µm biotin-coated bead and a 10.6 µm streptavidin-coated bead by the strong non-covalent biotin-streptavidin interaction. At time $t = 0$ s, both particles are trapped at two separate positions. Next, the target position for the bead on the left (biotin-coated) is slowly moved towards the target position for the bead on the right (streptavidin-coated). As the beads approach each other, both particles begin to deviate from their target positions, which is a consequence of interparticle hydrodynamic interactions [32, 41, 42]. Nevertheless, particles follow their target positions at all interparticle distances using the MPC algorithm. For assembly experiments, the controller weight parameter γ in the objective function (Eq. (3.6)) is increased slightly above the values used in two particle manipulation experiments described above, which amounts to a stricter penalization for not reaching the final target position. At $t = 95$ s, the two beads are firmly linked together

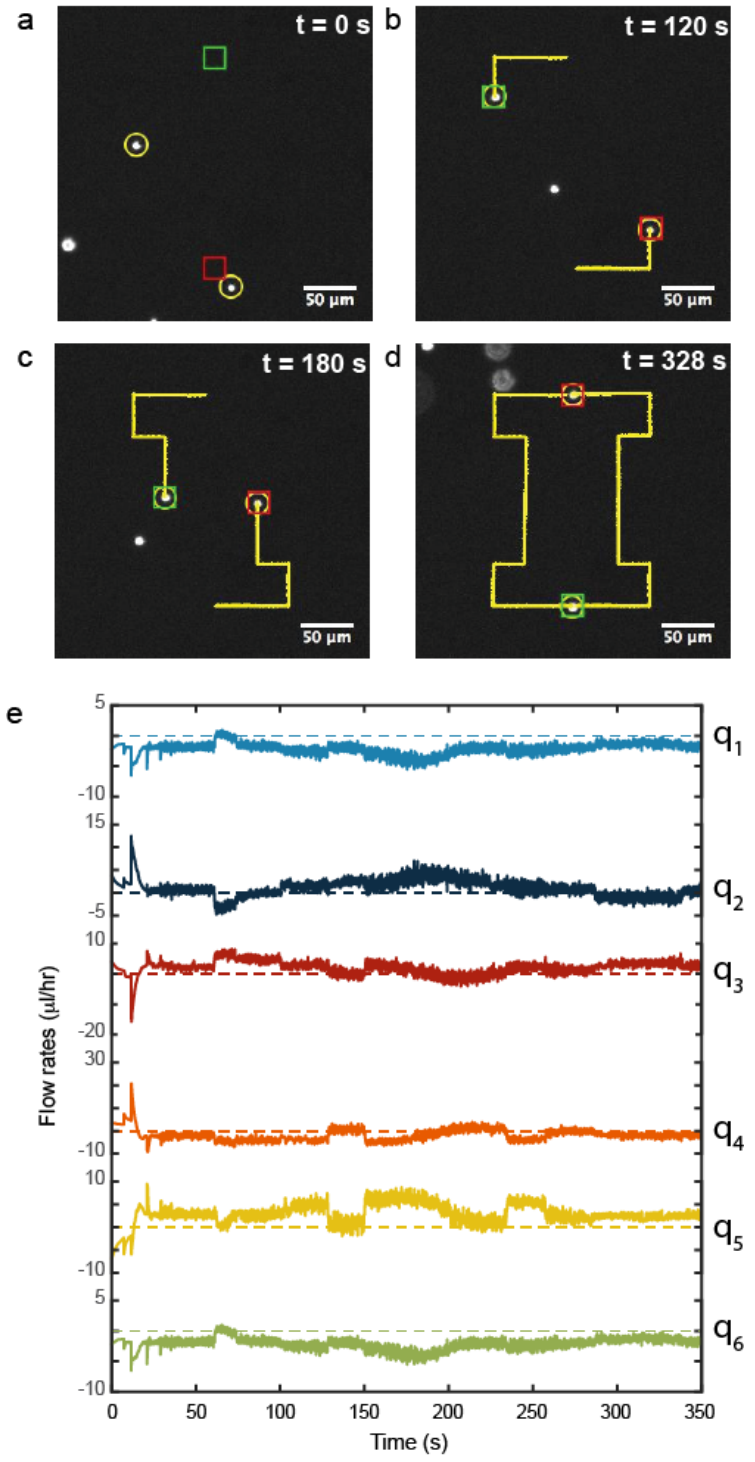

Figure 3.8: Manipulating two particles using the Stokes trap, where the objective is precisely control the paths of two 2.2 µm beads to trace the letter 'I'. (a)-(d) Snapshots of both particles at various instants of time, with the yellow line showing the past history of both particles. (e) Flow rates applied by the controller to the 6 inlet/outlet channels during the experiment.

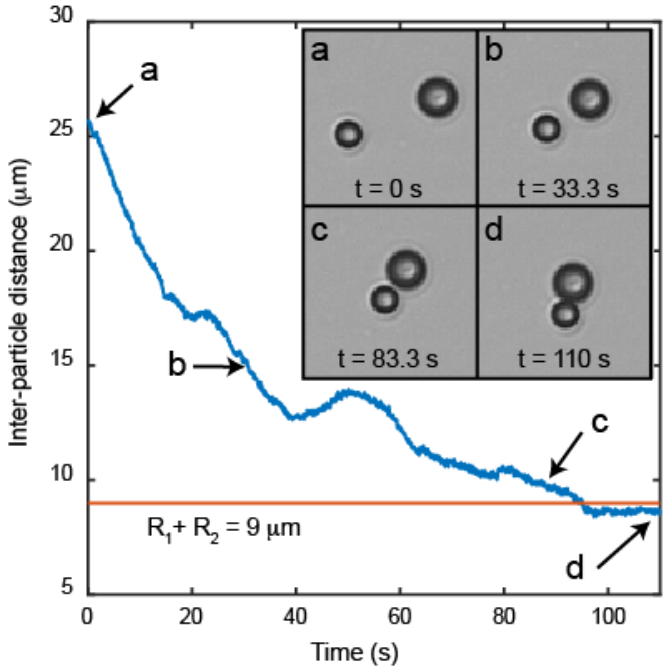

Figure 3.9: Fluidic-directed assembly of two particles using the Stokes trap. Interparticle distance is shown as a function of time during the assembly event between a 10.6 µm diameter streptavidin-coated bead and a 7.4 µm diameter biotin-coated bead. (Inset) Snapshots of both particles as a function of time, where points (a)-(d) correspond to the interparticle distance plot. The beads are successfully linked around 95 s.

by biotin-streptavidin interaction. The interparticle distance during the assembly event is plotted in Fig. 3.9, with snapshots of both particles shown in the inset. For reference, the expected interparticle distance after linking is also plotted on the same figure. After linking the two particles together, we moved the assembled structure around in solution to confirm that the beads were tightly linked.

3.4 Discussion

In this chapter, we demonstrate a new technique for manipulating and assembling microscale objects in free solution using the sole action fluid flow. We experimentally implement model predictive flow control, which greatly simplifies the microfluidic device design for trap-

ping by eliminating the need for integrated electrodes and on-chip membrane valves. The MPC algorithm is versatile and allows for the ability to control several particles independently, and as a proof of concept, we directly show the precise manipulation of two particles along arbitrary paths. We further use this technique to bring two particles in close contact, thereby facilitating linkage and directed assembly into a simple structure. Although simultaneous manipulation of multiple particles has been achieved using optical tweezers [3, 43] and electrokinetic traps [10], multiparticle manipulation and assembly mediated only by fluid flow has not yet been achieved.

A major advantage of the MPC algorithm is the ability to correct for model imperfections and system perturbations in a robust manner. For example, our simple fluidic model for fluid velocity (and particle velocity) is based on a linear superposition of two-dimensional point source flows around the perimeter of a polygonal flow cell. This model neglects interparticle hydrodynamic interactions, which give rise to perturbations in the fluid velocity that become significant upon close approach of the particles (*e.g.* when interparticle distance is less than $\sim$5 particle diameters). Nevertheless, as shown in the particle assembly experiment, the MPC algorithm is robust and successfully corrects limitations of the fluidic model.

A second advantage of implementing the MPC algorithm with distinct fluidic models is the ability to directly measure deviations of the system behavior from the model predictions. During an experiment, we record the transient and steady-state control input that effectively cancels any perturbations to the flow field. Interestingly, this approach allows for direct measurement of the fluid velocity arising from the flow field disturbances around trapped particles. In this manner, it should be possible to use one particle as a probe particle to record the fluid flow in the vicinity of a second particle. Thus, we believe that this technique can serve as a powerful tool to study interparticle interactions, including the direct measurement of the forces that arise during particle approach or collision events.

We further use the Stokes trap for the assembly of freely-suspended particles in solution, that is, for particles with no external force or torque couples (*e.g.* no external electric fields

or optical fields). In recent years, self-assembly of particles and molecules has been used to generate advanced functional materials with hierarchical structures [44]. The process of self-assembly, however, mainly relies on self-organization at thermal equilibrium [45–47]. From this perspective, it might be possible to access new levels of spatial ordering and hierarchical assembly by coupling external fields during the assembly process in a non-perturbative fashion. In the past, directed assembly of colloidal particles has been achieved by using external electrical fields [48, 49], acoustic fields [50], or optical fields [51]. Nevertheless, not all techniques are well-suited for directed assembly. Particle assembly with electrokinetic traps has been shown to be difficult, where the electrode potentials (voltages) required for bringing two 5 µm particles in contact diverged upon close approach, and as a consequence, these particles could not be brought closer than ∼8 µm [10]. Moreover, during any assembly event, the applied force fields should be non-pertubative such that they do not alter the underlying system properties.

In this regard, flow-based techniques could offer several advantages for directed assembly. Fluidic confinement forces scale favorably and linearly with particle diameter R compared to R^3 for optical traps and magnetic tweezers, which implies that the forces required for trapping a small particles using fluidics are physically reasonable given typical experimental conditions [10]. In addition, coupling external optical and electrical fields into microfluidic devices often has associated side-effects such as secondary flows generation and localized heating [21, 52], which could complicate the study of biological molecules and cells using these methods.

In future work, it may be possible to use the Stokes trap to systematically build higher-order and more complex assemblies of particles. In the current version of the trap, we use $N = 6$ inlet/outlet channels, though it has been predicted that this can be scaled up to N = 10-15 while retaining controllability with physically reasonable flow rates [31]. In the short term, however, the current device with $N = 6$ control variables could be used to control the 2D center-of-mass position of two particles while simultaneously controlling

the orientation of one of the two particles. By adding one additional channel ($N = 7$), it would be straightforward to control the 2D orientation and center-of-mass position of two anisotropic particles.

Chapter 4

Disturbance estimation and nonlinear model predictive path following control

In Chapter 3, we discuss the development and application of the Stokes trap [18], which enables the multiplexed manipulation of particles using the sole action of fluid flow. This technique uses precisely controlled flow rates determined by a model predictive control algorithm (MPC) to confine multiple particles simultaneously. Using this method, we demonstrate the precise 2-D manipulation of two particles along arbitrary paths and also assembled two sticky particles into a simple structure.

In this chapter, we extend the capabilities of the Stokes trap with respect to its robustness and its versatility. First, we implement an extended Kalman filter to estimate incoming disturbances and remove the offset during the regulation of the particle position. Second, we integrate path following with the MPC algorithm to improve the path following speed. These improvements together will enable detailed studies involving the interactions between two trapped particles.

4.1 Controller formulation

The basic idea of the Stokes trap is to control the position of particle along a user-defined trajectory by manipulating the fluid flow field within the device (Fig. 4.1). We illustrate this idea with the following examples. Consider Fig. 4.1a, where the goal is to move the particle along the x axis. This can be accomplished by delivering fluid into the cross-slot through the left channel and removing the fluid from the right channel. This flow configuration imposes a rightward fluid velocity at the position of the particle that pushes the particle along the x-axis. Imposing a flow rate in the bottom channel with the top channel serving as the outflow channel results in the analogous motion of the particle along

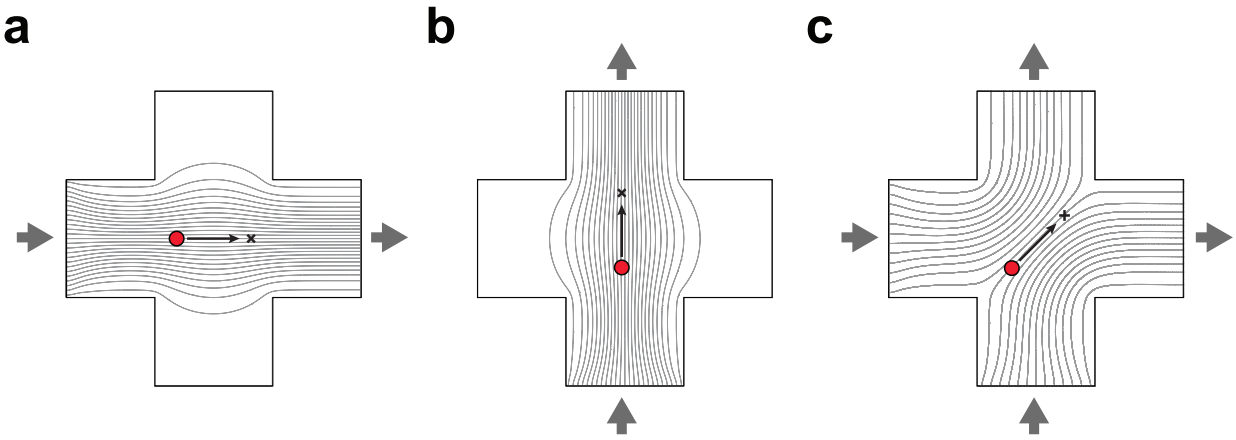

Figure 4.1: Using fluid flow to manipulate a single particle (the red circle) to a target position (the 'x' symbol). (a) The particle is moved along the x axis. The left channel is the inlet channel and the entire flow exits through the right channel. (b) The particle is moved along the y axis. The bottom channel is the inlet channel and the entire flow exits through the top channel. (c) Combined manipulation along the x and y axes. The flow enters through the left and bottom channels and exits through the top and right channels.

the positive y axis towards its target position (Fig. 4.1b). Finally, for manipulating both the x and y coordinates, we can combine the previous two cases, where the left and bottom channels behave as inflow channels and the top and right channels behave as the outflow channels. Changing the relative flow rate magnitudes for each channel (while preserving the mass conservation constraint for the net fluid entering the cross-slot) thus enables arbitrary control of both the x and y coordinates (Fig. 4.1c).

As we describe below, this control problem can be solved using model predictive control. We begin by first describing the model. As this model approximates the true flow field within the device, we next describe the application of extended Kalman filtering to account for model mismatch. In the following sections, we adopt the notation used in the control systems literature.

4.1.1 Model of particle flow

We first consider the fluid dynamics inside the microfluidic device. In low Reynolds number flow conditions, also known as Stokes flow, the inertial terms in the Navier-Stokes

equation can be neglected and we can write [42]:

$$0 = -\nabla p + \mu \nabla^2 u \tag{4.1}$$

where p is the dynamic pressure field, u is the velocity field, and μ is viscosity. In a microfluidic device cross-slot geometry generated by the intersection of N channels, we can approximate each channel as a two-dimensional point source. The final height averaged velocity field at a point x inside the cross-slot can then be approximated as a linear superposition of the velocity fields generated by each point source, as follows:

$$u = \frac{1}{\pi H} \sum_{i=1}^{N} \frac{(x - R^i) q_i}{\|x - R^i\|^2} \tag{4.2}$$

Here, H is the height of the device, $x \in \mathbb{R}^2$ is the position vector of the point, $R^i \in \mathbb{R}^2$ is the the position vector of the i^{th} point source, and $q \in \mathbb{R}^N$ is a vector whose i^{th} element represents the volumetric flow rate through the i^{th} point source. However, the flow rates q_i are not unconstrained, and must satisfy mass conservation. Hence, their algebraic sum must be 0:

$$\sum_{i=1}^{N} q_i = 0 \tag{4.3}$$

where flow rates are positive when they flow into the cross-slot and negative when they flow out. Together, Eqs. (4.2) and (4.3), completely determine the 2-D velocity field within the cross-slot geometry. In previous work, we performed a computational fluid dynamics simulation in COMSOL to compare the height averaged velocity with the velocity prediction from Eq. (4.2) [18]. We found that an appropriate choice of the channel height and width can reduce the error between the COMSOL velocity predictions and the point source velocity predictions to $\sim 2\%$.

In the absence of external forces, and neglecting inter-particle hydrodynamic interactions,

we can assume that a particle is advected with the local fluid velocity. In this case, we can model the particle's motion using the following equation:

$$\dot{x} = f(x, q) \triangleq \frac{1}{\pi H} \sum_{i=1}^{N} \frac{(x - R^i)q_i}{\|x - R^i\|^2} \tag{4.4}$$

4.1.2 Model predictive control formulation

In the superposed point source velocity field of Eq. (4.4), our objective is to manipulate a single particle, a task that poses several experimental challenges. First, we seek to manipulate micron sized particles, which are subject to Brownian motion, and thus follow non-deterministic trajectories. Additionally, the fluidic model described in Eq. (4.2) is an approximation, and any control strategy must be sufficiently robust to handle unmodelled behavior. Finally, the positions of the particle are sampled at 30 Hz, hence the control strategy should be capable of calculating the optimal control law within 33 ms. For these reasons, we use model predictive control (MPC) to precisely manipulate the particle [33].

Consider the task of manipulating a single particle from the point x_0 to the point x_F. Although there are infinitely many trajectories between these points, we would like to select a trajectory that simultaneously minimizes the flow rates as well as the distance traveled. We can systematically obtain these trajectories and the corresponding flow rates at each sampling instant by minimizing the following objective:

$$\begin{aligned}
\min_{\tilde{x},\tilde{q}} J = & \sum_{\tau=t_k}^{t_k+T_M-1} \left\{ \alpha \left(\|\tilde{x}(\tau) - x_F\|^2 \right) + \beta \|\tilde{q}(\tau)\|^2 \right\} \\
& + \gamma \left(\|\tilde{x}(t_k + T_M) - x_F\|^2 \right) && \text{(4.5a)} \\
\text{s.t.} \quad & \frac{d\tilde{x}}{dt} = f(\tilde{x}, \tilde{q}), \quad \tilde{x}(t_k) = x(t_k) && \text{(4.5b)} \\
& \sum_{i=1}^{N} \tilde{q}_i(\tau) = 0 \quad \forall\ \tau = t_k, \ldots, t_k + T_M && \text{(4.5c)}
\end{aligned}$$

Here, $t_k = t_0 + k\Delta$ represents the k^{th} sampling instant and T_M is the MPC horizon, consisting

of M regular intervals such that $T_M = M\Delta$, where Δ is the sampling interval. $\tilde{x}(\tau)$ indicates the predicted value of the position at time τ, whereas $\tilde{q}(\tau)$ indicates the predicted piecewise constant control applied during the interval $[\tau, \tau + \Delta)$. α, β and γ are the controller weights which are tuned during the manipulation experiment to obtained the desired performance. Following the MPC strategy, we minimize the objective function in Eq. (4.5) every sampling instant to obtain the flow rates over the entire horizon, but we only apply the flow rates corresponding to the first MPC interval by setting $q(t_k) = \tilde{q}(t_k)$ and resample the position of the particle x at the next sampling instant. Here, we use the toolkit for Automatic Control and Dynamic Optimization (ACADO) for implementing experimental MPC [34, 36].

4.1.3 Extended Kalman Filter

The point source velocity model (Eq. (4.2)) is an approximation to the actual 3-D velocity field. Moreover, the actual velocity inside the cross-slot might depart significantly from Eq. (4.4) because of incoming disturbances. These disturbances arise from inaccuracies in the imposed flow rates and irregularities in the microfluidic channels caused due to variations in the photolithography process. In these conditions, the controller formulation discussed previously is unable to achieve offset free regulation of the particle position.

For these reasons, we implement an extended Kalman filter (EKF) to estimate the disturbance velocity p [53]. We begin by augmenting the system of Eq. (4.4) with an additional state $p \in \mathbb{R}^2$ representing the input disturbance:

$$\begin{aligned}
\dot{z} \triangleq \begin{bmatrix} \dot{x} \\ \dot{p} \end{bmatrix} &= \begin{bmatrix} f(x,q) + p \\ 0 \end{bmatrix} + \begin{bmatrix} 0 \\ I_2 \end{bmatrix} \omega \\
&= g(z,q) + G\omega \qquad (4.6a) \\
y(k) = \begin{bmatrix} I_2 & 0 \end{bmatrix} z(k) &+ w(k) \\
&= Cz(k) + w(k) \qquad (4.6b)
\end{aligned}$$

where I_n denotes an identity matrix of rank n, $z \in \mathbb{R}^4$ is the augmented system state, $\omega(t) \in \mathbb{R}^2$ is the input noise which is a normal random vector with zero mean and known covariance matrix $Q \in \mathbb{R}^{2\times 2}$. $y(k)$ represents the measurement of the position of the particle at sampling instance t_k, while $w(k) \in \mathbb{R}^2$ is the input measurement noise which is a normal random vector with zero mean and covariance matrix $S \in \mathbb{R}^{2\times 2}$.

Let $\hat{z}_m(k)$ and $\hat{P}_m(k) = E[(z(k) - \hat{z}_m(k))(z(k) - \hat{z}_m(k))^T]$ represent an approximation of the conditional mean and variance of the true state $z(k)$ given the measurements $\{y(i)\}_{i=1}^k$, and we initialize them as $\hat{z}_m(0) = z_0$ and $\hat{P}_m(0) = P_0$. We denote the prior estimate of the state and the state variance matrix as $\hat{z}_p$ and $\hat{P}_p$. Then, the prior values $\hat{z}_p(k)$ and $\hat{P}_p(k)$ are calculated by solving the following equations in the interval $[t_{k-1}, t_k]$ to obtain their values at sampling instant t_k:

$$\dot{z}(t) = g(z(t), q),\ z(t_{k-1}) = \hat{z}_m(k-1) \tag{4.7a}$$

$$\dot{P}(t) = A(t)P(t) + P(t)A^T(t) + GQG^T, P(t_{k-1}) = \hat{P}_m(k-1) \tag{4.7b}$$

where

$$A(t) = \frac{\partial G(z,q)}{\partial z} = \begin{bmatrix} \frac{1}{\pi H}\sum_{m=1}^{N}\left[\frac{I_2}{\|x-R^m\|^2} - \frac{2(x-R^m)(x-R^m)^T}{\|x-R^m\|^4}\right] q_m & I_2 \\ 0 & 0 \end{bmatrix}$$

Finally, $y(k)$ is measured, and the *a posteriori* update is done as follows:

$$K(k) = \hat{P}_p(k)C^T[C\hat{P}_p^T(k)C^T + S]^{-1} \tag{4.8a}$$

$$\hat{z}_m(k) = \hat{z}_p(k) + K(k)[y(k) - C\hat{z}_p(k)] \tag{4.8b}$$

$$\hat{P}_m(k) = [I_4 - K(k)C]\hat{P}_p(k) \tag{4.8c}$$

The EKF operates in conjunction with an MPC controller identical to the one discussed

in Eq. (4.5), except that instead of the system model in Eq. (4.5b), we use the following system model using the estimate of $p(t_k)$ from the EKF:

$$\frac{d\tilde{x}}{dt} = f(\tilde{x}, \tilde{q}) + p(t_k), \quad \tilde{x}(t_k) = x(t_k)$$

4.1.4 Path following

In previous work, we have demonstrated the precise manipulation of a micron sized particle along a preprogrammed path [18]. However, in that implementation, the set point was stepped along the path at a constant speed without considering the position of the particle. In some cases, the particle would be far away from the setpoint when the setpoint value was changed to the next position, and the particle would deviate from the reference trajectory while moving towards the setpoint.

Addressing this issue requires coordinating the setpoint motion with the motion of the particle, so that the setpoint speed along the trajectory can be increased or decreased based on the lag distance of the particle. Here we implement nonlinear model predictive path following control as described in [54].

We parameterize the reference trajectory r using a parameter θ such that $r(\theta) : [-1, 0] \mapsto \mathbb{R}^2$ represents the desired trajectory. The MPC formulation in Eq. (4.5) is modified as follows:

$$\min_{\tilde{x},\tilde{q},\theta} J = \sum_{\tau=t_k}^{t_k+T_M-1} \Big\{\alpha\|\tilde{x}(\tau) - r(\tilde{\theta})\|^2 + \delta_1\|\tilde{\theta}(\tau)\|^2 + \beta\|\tilde{q}(\tau)\|^2 \tag{4.9a}$$

$$+ \delta_2\|\phi(\tau)\|^2\Big\} + \gamma(\|\tilde{x}(t_k + T_M) - r(\tilde{\theta}(t_k + T_m))\|^2 + \|\tilde{\theta}(t_k + T_m)\|^2)$$

$$\text{s.t. } \frac{d\tilde{x}}{dt} = f(\tilde{x}, \tilde{q}), \quad \tilde{x}(t_k) = x(t_k) \tag{4.9b}$$

$$\dot{\tilde{\theta}} = -\lambda\tilde{\theta} + \Phi_{max} - \phi, \quad \tilde{\theta}(t_k) = \theta(t_k|\theta(t_{k-1})) \tag{4.9c}$$

$$0 \leq \tilde{\phi}(\tau) \leq \Phi_{max} \tag{4.9d}$$

$$\sum_{i=1}^{N} \tilde{q}_i(\tau) = 0 \quad \forall\ \tau = t_k, \ldots, t_k + T_M \tag{4.9e}$$

Equation (4.9c) is known as the timing law since it controls the evolution of the path parameter θ. λ is a small value (typically $\sim 10^{-5}$) which is used to stabilize the timing law, ϕ is the speed of the setpoint along the reference trajectory, and Φ_{max} denotes the maximum permissible value of ϕ. Φ_{max} can be tuned based on how fast the reference trajectory must be tracked. At every sampling instant, the initial condition for $\tilde{\theta}$ is set equal to the predicted value of θ from the previous sampling instant, based on the timing law with θ being set to -1 for the first sampling instance corresponding to the beginning of the path.

4.2 Experimental Implementation

4.2.1 Experimental setup

The setup consists of 4 pressure regulators which pressurize distinct fluidic reservoirs to control the flow rates q through each channel, as shown in Fig. 4.2a. These fluidic reservoirs are connected to the microfluidic device using FEP tubing. The microfluidic device is mounted on the stage of an inverted microscope (Olympus IX71) which is equipped with a 10x magnification objective and a CCD camera. For all manipulation experiments we use 2.2 µm Nile Red fluorescent polystyrene beads suspended in an aqueous glycerol solution

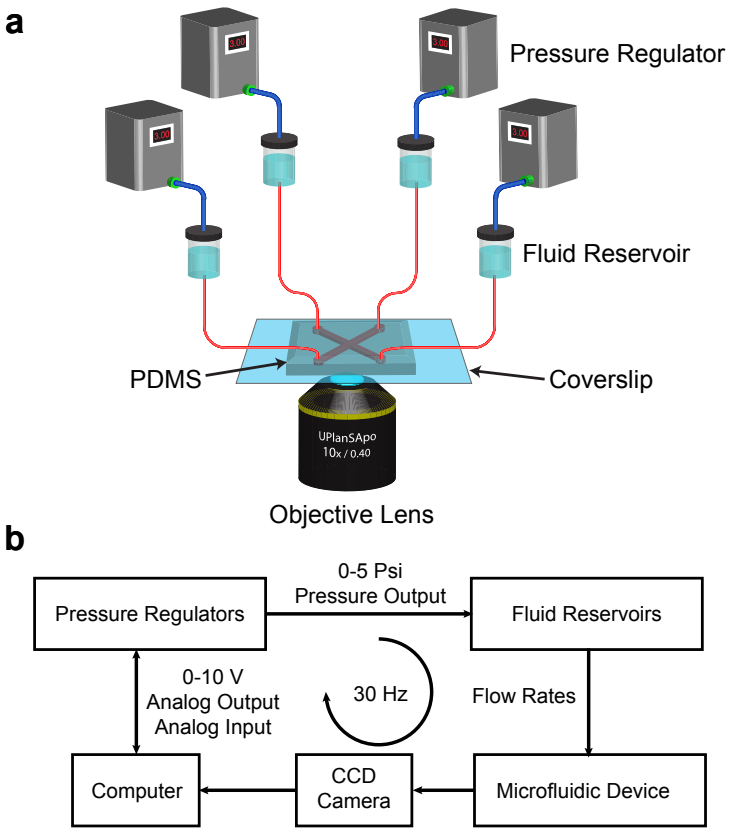

Figure 4.2: Overview of the Stokes trap and control algorithm. (a) Overview of the experimental setup. Inlet/outlet channels in the 4 channel microfluidic device are connected to 4 fluidic reservoirs that are pressurized by regulators controlled by a custom LabVIEW program. The fluidic reservoirs deliver the required amount of flow rates into the device. (b) Block diagram of the control loop for particle manipulation.

with a viscosity of 0.140 Pa-s measured at 22°C.

4.2.2 Controller implementation

A schematic of the control loop is shown in Fig. 4.2b. A custom LabVIEW code interfaced with the ACADO package is used for particle manipulation. The control loop begins with the acquisition of an image by the CCD Camera which relays it to the LabVIEW program. Next, LabVIEW determines the 2-D center-of-mass coordinates for the particle of interest and relays these coordinates to the ACADO controller. The ACADO controller solves Eq. (4.5)

to determine the optimal flow rate values q, and sends these values back to LabVIEW. Finally, LabVIEW converts the flow rates to pressure values and actuates the pressure regulators which deliver the required flow rates into the microfluidic device, after which the entire control loop repeats again. In typical experiments, this control loop operates at 30 Hz. The EKF is implemented in MATLAB and interfaces with the LabVIEW code described above.

For obtaining the corresponding pressure values for flow rates q_i provided by the MPC algorithm, we convert the entire setup into a fluidic circuit, with each fluid reservoir acting as a pressure source. The fluidic path from the fluid reservoir to the cross-slot through the i^{th} channel is associated with a hydrodynamic resistance Z_i. We assume that the center of the cross-slot is at an average pressure P_0, which allows us to calculate the pressure P_i to be applied on the i^{th} reservoir using the following equation:

$$P_i = P_0 + q_i Z_i \tag{4.10}$$

4.2.3 Microfluidic device geometry and dimensions

We use a $N = 4$ channel microfluidic device with a channel width of $\sim 400\ \mu m$ and a channel height of $\sim 100\ \mu m$ (Fig. 4.3a,b). The junction of these channels forms a square with a side $W = 400\ \mu m$. The microfluidic device is aligned so that the center of the cross-slot junction is at the origin of the laboratory reference frame. Then the point sources corresponding to the 4 channels are assumed to be on the inscribed circle of the square as follows:

$$R = \frac{W}{2} \tag{4.11}$$

$$R^i = R\left[\cos\left((i-1)\frac{\pi}{2}\right), \sin\left((i-1)\frac{\pi}{2}\right)\right]^T \tag{4.12}$$

The locations of the 4 point sources have been shown in Fig. 4.3b.

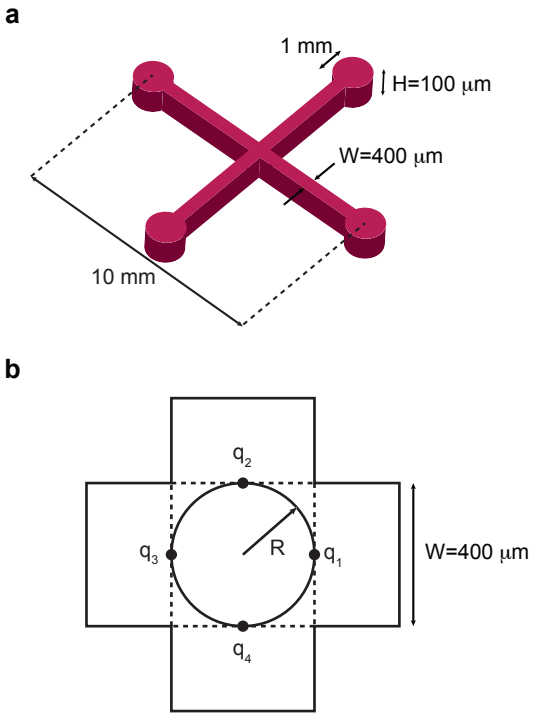

Figure 4.3: Microfluidic device geometry (a) Schematic showing the height, width and length of the microfluidic channels. (b) Schematic showing the location of the point source corresponding to each channel.

4.2.4 Scaling and dimensionless equations

To effectively minimize the objective function without encountering underflow, we scale all parameters so that they are roughly $O(1)$. We choose the particle diameter $d = 2.2$ µm as the length scale, and the inverse of the characteristic strain rate $\dot{\varepsilon}^{-1} = 1$ as the time scale (the strain rate is the eigenvalue of the gradient of velocity tensor,∇u), which leads to a flow rate scale $q_S = \pi \dot{\varepsilon} d^2 H$. We scale all lengths, times and flow rates in Eq. (4.4) and use $\bar{\cdot}$ to indicate the corresponding dimensionless quantities:

$$\dot{\bar{x}} = \bar{f}(\bar{x}, \bar{q}) \triangleq \sum_{i=1}^{N} \frac{(\bar{x} - \bar{R}^i)\bar{q}_i}{\|\bar{x} - \bar{R}^i\|^2} \tag{4.13}$$
$$\bar{t} = \dot{\varepsilon} t,\ \bar{x} = \frac{x}{d}, \bar{R}^i = \frac{R^i}{d},\ \bar{q} = \frac{q}{q_S}$$

4.3 Results

4.3.1 Trapping a single particle

In this experiment, a single 2.2 µm particle was trapped at the origin of the cross-slot, i.e. $\bar{x}_F = 0$. The controller weights were set to $\alpha = 1$, $\beta = 10^{-5}$ and $\gamma = 1$, with $P_0 = 2.5$ Psi. Fig. 4.4a,b shows the x and y coordinates of the particle over a period of 30 s, in addition to the reference position. During the experiment, a time varying offset was observed for both the x and y coordinates, with an average value of 0.19 µm for the x coordinate and 0.38 µm for the y coordinate. This offset arises because of unmodeled disturbances within the cross-slot, such as asymmetric resistances in the four fluidic paths. These unmodeled disturbances are not known *a priori* and they might change from one experiment to the next experiment as they are affected by the particular manner in which the microfluidic tubing is connected to the device in addition to irregularities in the device features.

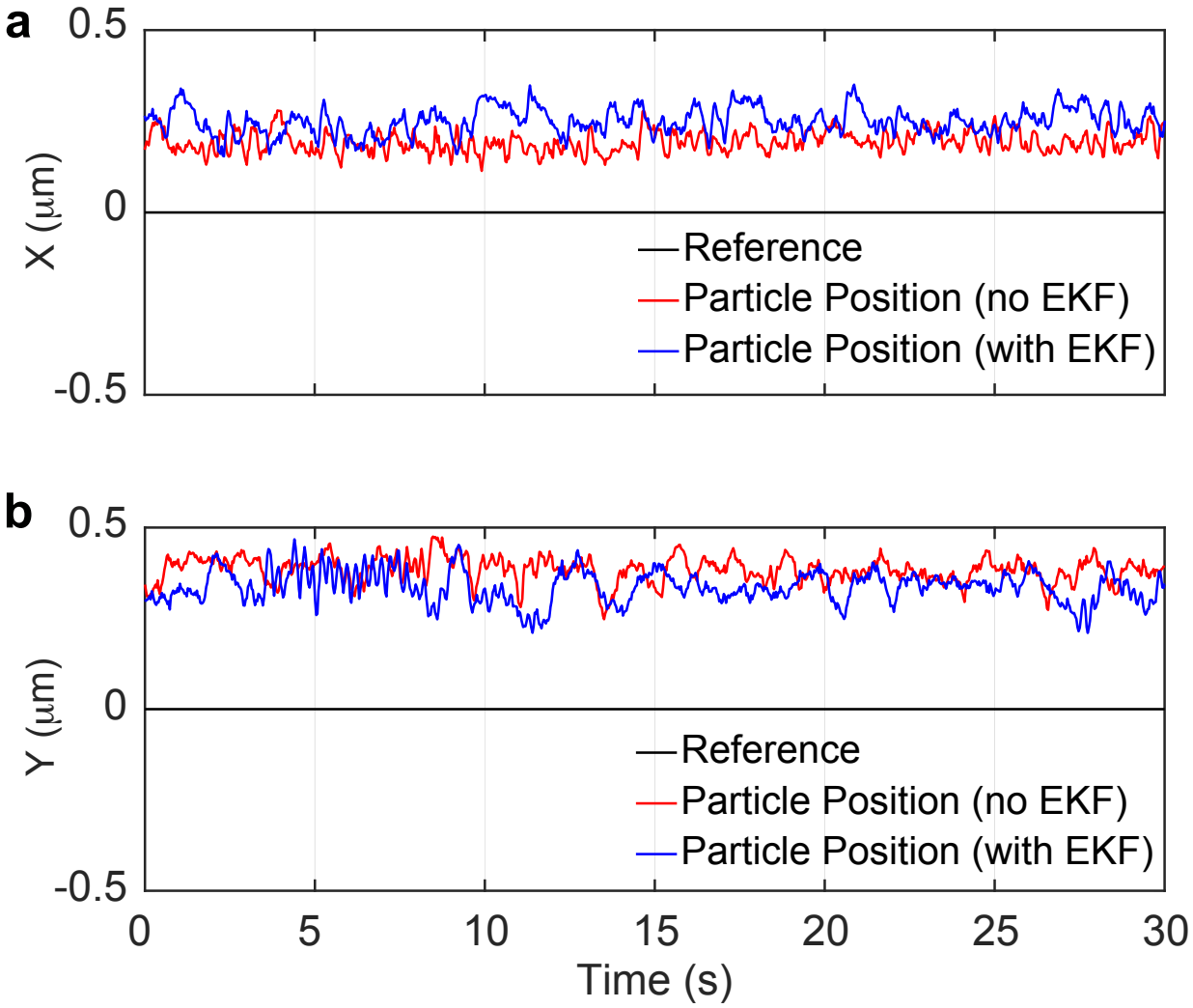

Figure 4.4: Trajectory of a particle trapped at the origin (a) The x coordinate of the particle as a function of time, with and without the EKF. In this case, since the particle's offset is already small, adding the EKF does not result in significant improvement. (b) The y coordinate of the particle as a function of time, with and without the EKF.

4.3.2 Implementing the EKF

To estimate these disturbances during the experiment, and remove the offset, we implemented the extended Kalman filter (EKF) described in Section 4.1.3. The controller weights were maintained at the same value, while the process noise and measurement noise matrices were set to $Q = 0.1I_2$ and $S = 0.1I_2$ respectively. As shown in Fig. 4.4a,b, after the implementation of the EKF, the mean offset in the x coordinate is 0.25 µm, while the mean offset in the y coordinate is 0.34 µm. In this case, the introduction of the EKF does not lead to an improvement since the original offsets are comparable to the uncertainty in locating the center-of-mass coordinates of the particle ($\sim$ 200 nm). Figure 4.5 compares the x and y coordinates of the particle obtained from Labview to the coordinates obtained by running a more rigorous particle localization algorithm using ImageJ [37]. During the experiment, the coordinates obtained from Labview are used, and as shown in Fig. 4.5, both the coordinates have a nearly zero mean value, indicating that the EKF is indeed able to regulate the particle's position with zero offset. However, it is clear that there is a significant error in estimating the position of the particle since there is on average a difference of 0.3 µm in the estimates obtained from Labview and ImageJ. Thus, by implementing a more accurate algorithm for estimating the position of the particle during the experiment and using those coordinates with the EKF, we can successfully estimate an arbitrary incoming disturbance and cancel its effect on the motion of the particle.

4.3.3 Path following

We also implemented path following as discussed in Section 4.1.4. In this experiment, the controller weights were set to $\alpha = 1$, $\beta = 10^{-5}$, $\gamma = 1.0$, $\delta_1 = 10^6$ and $\delta_2 = 10^{-5}$. The cross-slot pressure was set to $P_0 = 0.9$ Psi.

We traced a 'Figure 8', whose parametric equation is $r(\theta) = [30\cos(-2\pi\theta),\ 15\sin(-4\pi\theta)]^T$, with $\theta \in [-1, 0]$. We set $\lambda = 10^{-5}$ and $\Phi_{max} = 0.05$. Figure 4.6 shows the reference trajectory overlaid with the actual trajectory of the particle and it is seen that the particle follows

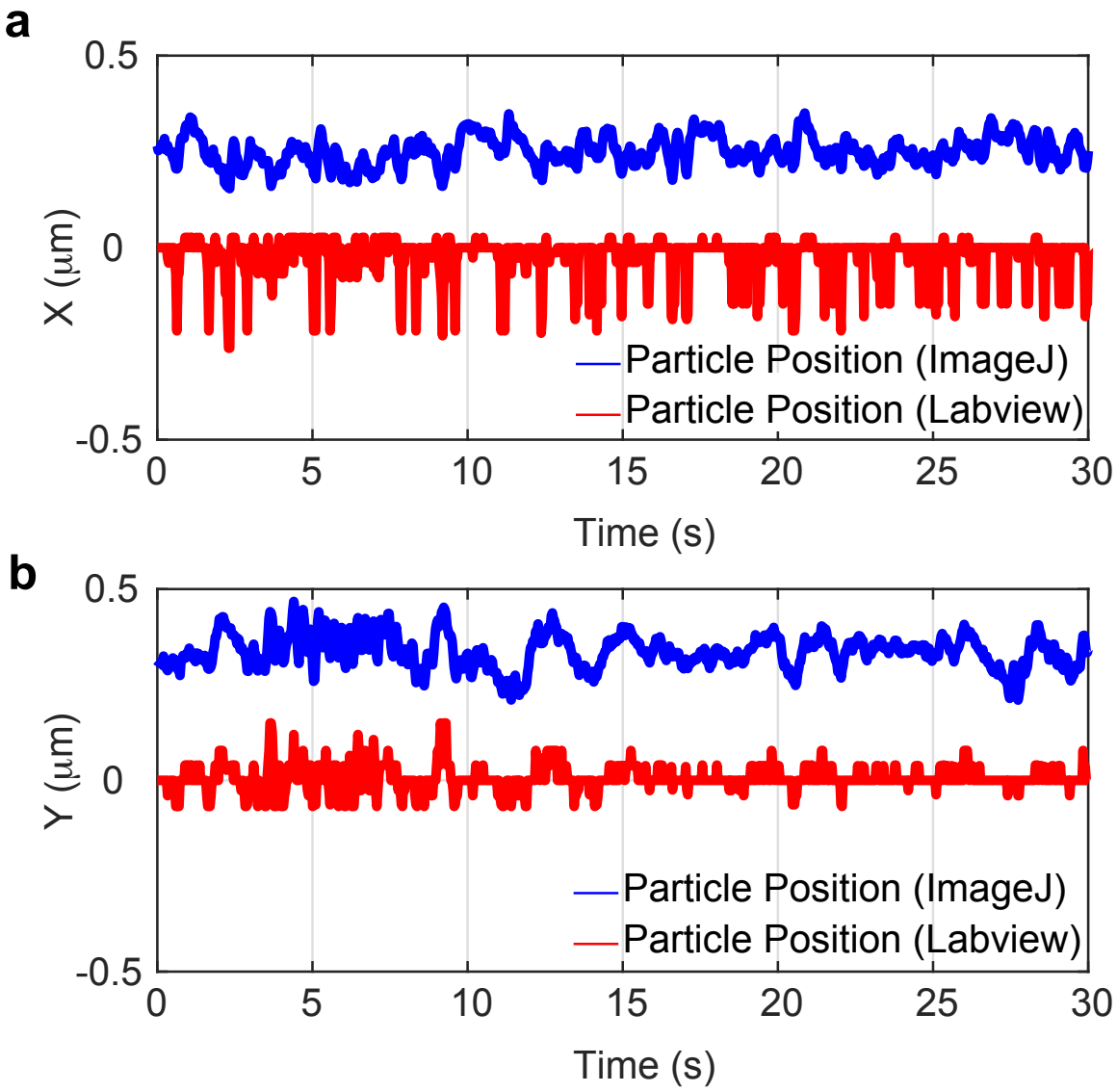

Figure 4.5: A comparison between the x and y coordinates of a particle as detected by Labview and ImageJ. (a) The x coordinate of the particle as a function of time and (b) the y coordinate of the particle as a function of time.

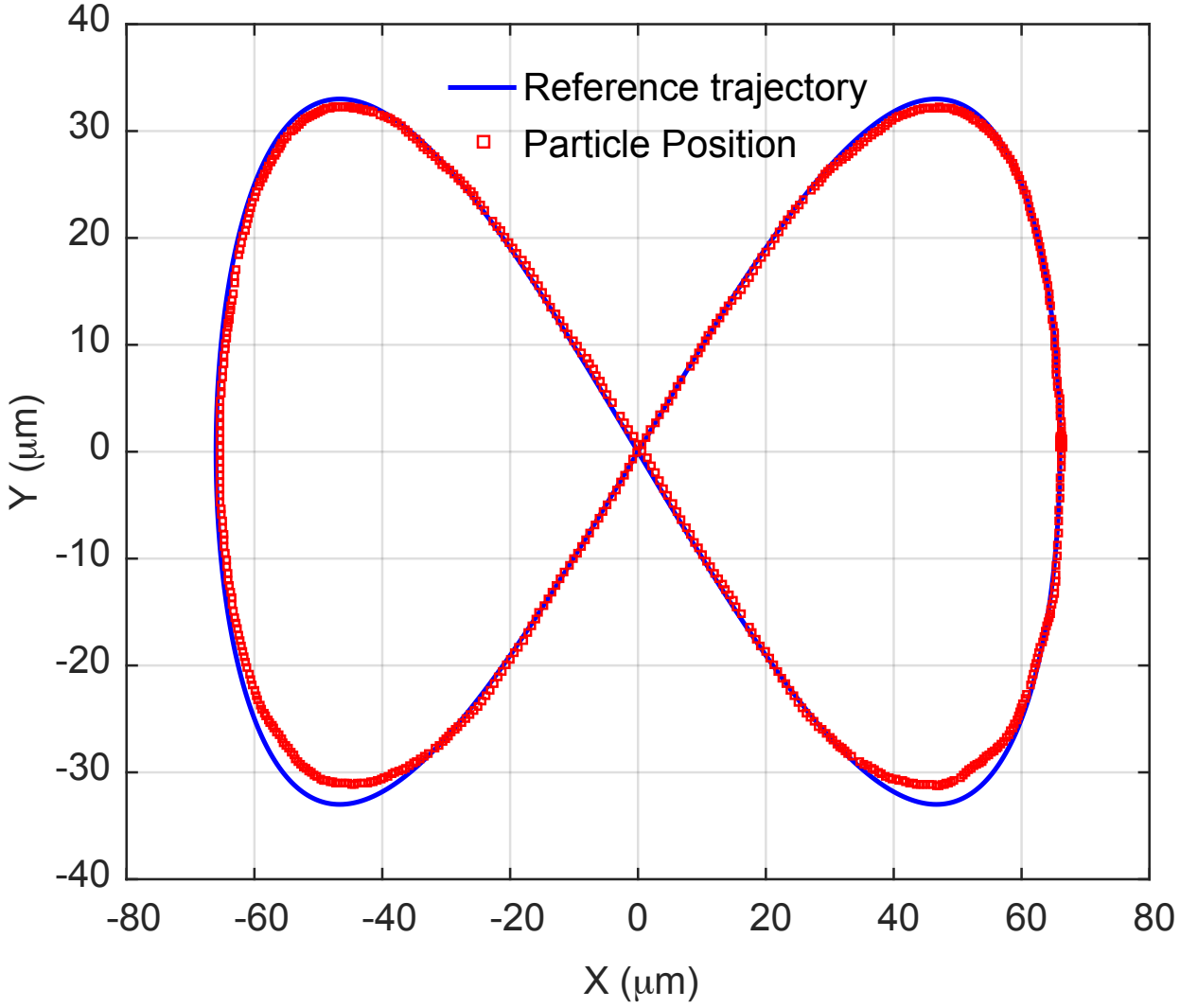

Figure 4.6: A trapped particle traces a 'Figure-8' curve. The reference trajectory has been shown in blue, with the red squares marking the position of the particle at different times.

the reference trajectory fairly closely and the deviations from the reference trajectory are small. Figure 4.7a,b shows the evolution of the individual coordinates x and y of the particle. Again, we see that the particle follows the reference trajectory with small perturbations (less than the particle diameter, d = 2.2 µm). More importantly, the particle is able to cover a large distance of $\sim 300\mu$m within a short period of time (∼20 s). This represents a dramatic improvement over our previous approach of moving the setpoint at a fixed speed where it took ∼300 s to cover a distance of ∼ 200 µm.

The errors shown in Fig. 4.7c,d represent the difference between the setpoint position and the particle's position, but not the distance between the particle's position and its projection onto the reference trajectory. Thus, even though the errors shown in Fig. 4.7c,d have an absolute value of around 1 µm for the x coordinate and y coordinate, the projected errors are lower since in many cases the particle lags behind the setpoint but stays on the curve. This is clearly observed in Fig. 4.7c,d, where the errors in x and y coordinates are correlated with the x and y coordinates of the trajectory shown in Fig. 4.7a,b. When the particle is stationary, i.e. during the period 0-8 seconds, and 30-40 s, the error corresponds to a value of roughly 0.2 µm which can be attributed to an error in localizing the position of the particle in Labview, as shown in Fig. 4.5. When the particle moves, the particle lags behind the setpoint, which leads to a positive value of the error when the setpoint's x or y coordinate is positive and a negative value for the error when the setpoint's x or y coordinate is negative. Indeed, we see this effect manifested in Fig. 4.7c,d where the errors in the x and y coordinates are correlated with the x and y components of the particle's trajectory, and the large value of the errors occur when the setpoint moves through the curved section of the 'Figure-8' trajectory. In these curved sections, the particle tries to follow a straight line path to the setpoint, and since it generally lags behind the setpoint, this causes the particle to deviate from the ideal trajectory (as shown in Fig. 4.6 near the two curved sections at the bottom of the 'Figure-8'). These errors can be reduced further by appropriately tuning the weights corresponding to the difference between the setpoint and the particle's position

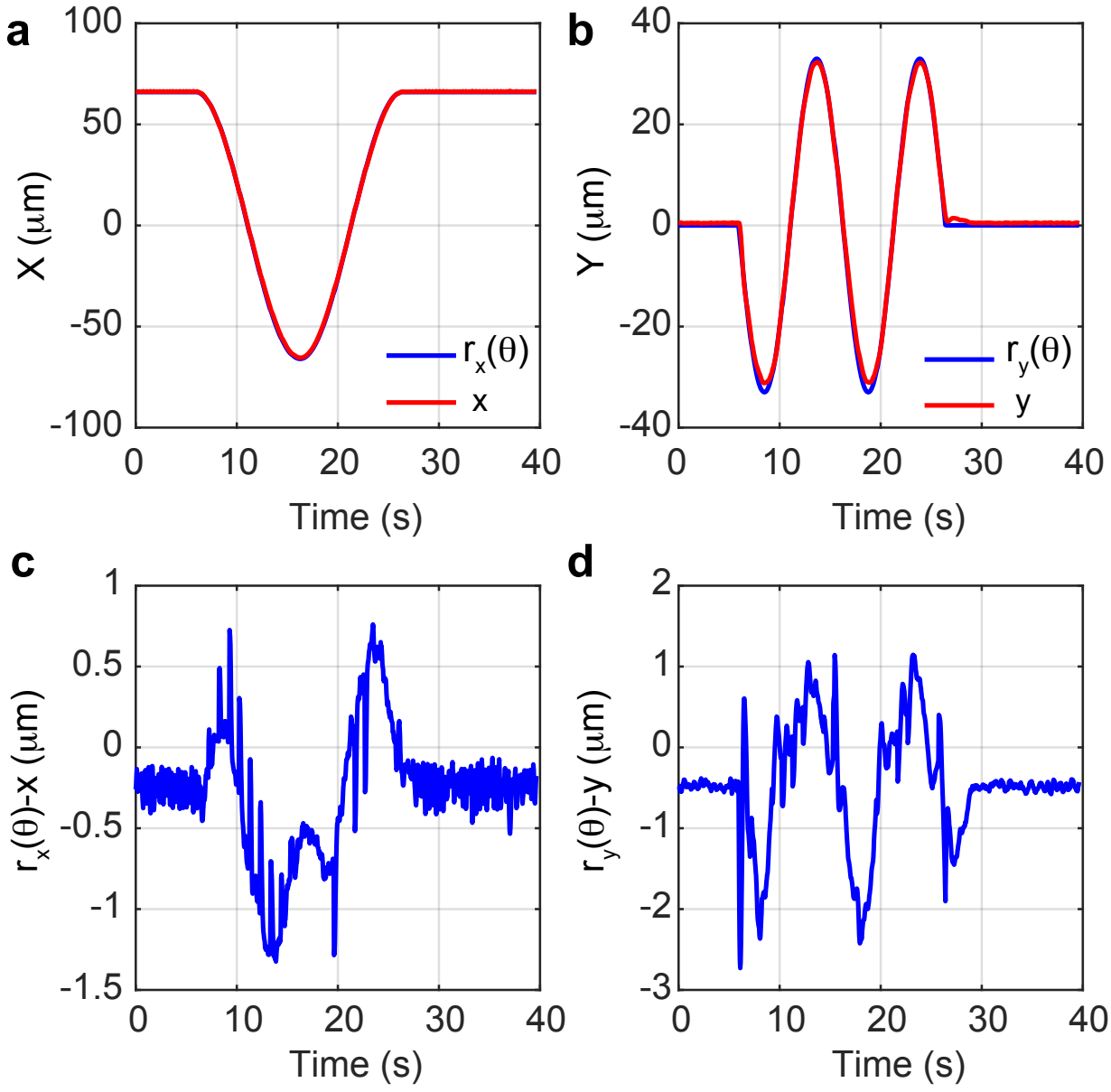

Figure 4.7: The reference and the actual trajectory of the particle during path following. (a) x coordinate of the particle and the reference trajectory as a function of time, (b) y coordinate of the particle and the reference trajectory as a function of time, (c) the error between the x coordinate of the particle and the x coordinate of the reference trajectory as a function of time and (d) the error between the y coordinate of the particle and the y coordinate of the reference trajectory as a function of time.

and the weights corresponding to the flow rates q.

4.3.4 Measuring the velocity field induced by hydrodynamic interactions

In prior work (Chapter 3), we have established that a careful choice of the device height and channel width allows the error between the height averaged 3-D velocity field and the 2-D Hele Shaw velocity to be reduced to $\sim$2%. In such a microfluidic device, when the distance between the two trapped particles is much greater than the particle diameter, and hydrodynamic interactions are negligible, the model predictive control algorithm is able to accurately predict the dynamics of each particle, and precisely manipulate both particles along a user-defined trajectory. On the other hand, when the distance between the trapped particles is comparable to the particle diameter, hydrodynamic interactions become important, and this adds an extra disturbance velocity term to the original equation for the velocity of a single particle in the Hele Shaw flow field. As a consequence, the actual motion of the particles is no longer governed by the model used by the controller, and when the particles are brought in close proximity to each other, they start deviating from their set point position.

In this case, a careful retuning of the controller weights is then necessary to remove the offset between the desired location of the particle and the actual position. Previously, we used an integrator to remove experimental offset, but it is well known that adding an integrator leads to a loss of stability. Developing an alternative method of removing offset and estimating this disturbance velocity will not only enable the elimination of position offset, but will also facilitate the direct measurement of the disturbance velocity field experienced by both particles.

Here, we will use the EKF developed in the previous sections to measure the hydrodynamic interactions between two particles suspended in a Newtonian fluid. First, we consider a single sphere suspended in the velocity field described by Eq. (4.2). Assuming that the center of mass of the particle is at x_0, we expand the undisturbed velocity field (i.e. the

velocity field in the absence of the particle) around the center of mass of the particle as follows:

$$u^{\infty}(x) = u^{\infty}(x_0) + (\nabla^T u^{\infty})|_{x_0}(x - x_0) + \frac{(x - x_0)^T \nabla^2 u^{\infty}|_{x_0}(x - x_0)}{2} + \dots \tag{4.14}$$

However, all terms beginning from third term are 0, since $\nabla^2 u^{\infty} = 0$ for the velocity field in Eq. (4.4). This is because the velocity field is a superposition of the velocities driven by point sources. Point sources are singularity solutions of the Stokes equation (Eq. (4.1)) associated with a constant or zero pressure field, implying $\nabla p = 0$, so that the Eq. (4.2) becomes $\nabla^2 u = 0$. Additionally, the velocity field due to a point source is purely extensional in nature, so that the gradient of velocity tensor ∇u^{∞} is symmetric, and thus equal to the rate of strain tensor E^{∞}. This leads to the following expression

$$\begin{aligned} u^{\infty}(x) &= u^{\infty}(x_0) + E^{\infty}_{ij}|_{x_0}(x - x_0) \\ E^{\infty}_{ij} &= \frac{1}{2}\left(\frac{\partial u_i}{\partial x_j} + \frac{\partial u_j}{\partial x_i}\right) \end{aligned} \tag{4.15}$$

Equation (4.15) is a superposition of a uniform flow (the first term) and extensional flow (the second term). Hence, the total disturbance velocity generated by a freely suspended sphere in this flow can be determined by obtaining the disturbance flow for each term, and then superposing them. For a sphere immersed in uniform flow and moving with the velocity of the undisturbed flow, the disturbance velocity field is identically zero. For the second term, we observe that the undisturbed velocity field is driven by a rate of strain tensor E which is symmetric, hence the disturbance velocity must have contributions from a potential quadrupole and a stresslet, since these singularities have second order tensorial constants [42]. Let $\hat{x}$ denote the position vector from the point x_0 to the point x, with its

magnitude given by $\hat{r} = \sqrt{\hat{x}_l \hat{x}_l}$. The disturbance velocity is thus:

$$u_i^D = \underbrace{\frac{1}{4\pi} Q_{ijl}\ q_{jl}}_{\text{Potential quadrupole}} + \underbrace{\frac{1}{8\pi\mu} \Sigma_{ijl}\ p_{jl}}_{\text{Stresslet}} \tag{4.16a}$$

$$Q_{ijl} = -3\frac{(\delta_{ij}\hat{x}_l + \delta_{jl}\hat{x}_i + \delta_{li}\hat{x}_j)}{\hat{r}^5} + 15\frac{\hat{x}_i\hat{x}_j\hat{x}_l}{\hat{r}^7} \tag{4.16b}$$

$$\Sigma_{ijl} = 3\frac{\hat{x}_i\hat{x}_j\hat{x}_l}{\hat{r}^5} \tag{4.16c}$$

where μ is the viscosity of the fluid.

Finally, we need to determine the constants q_{jl} and p_{jl}. We note that the total velocity must satisfy no slip on the surface of the sphere and the disturbance velocity must decay to 0 at a large distance from the sphere. e_l denotes the position vector of an arbitrary point on the surface and a is the radius of the sphere. The boundary conditions for the velocity field are then:

$$u_i^D = -u_i^\infty \quad \text{at} \quad \hat{x}_l = a e_l \tag{4.17}$$

$$u_i^D = 0 \quad \text{at} \quad \hat{x}_l \to \infty \tag{4.18}$$

This leads to the following values for q_{jl} and p_{jl}:

$$q_{ij} = \frac{2\pi a^5}{3} E_{ij}^\infty \tag{4.19}$$

$$p_{ij} = -\frac{20\mu\pi a^3}{3} E_{ij}^\infty \tag{4.20}$$

The disturbance velocity field and the total velocity field is

$$u_i^D(x) = -E_{ij}^\infty x_j \frac{a^5}{r^5} + \frac{5}{2} x_i x_j x_k E_{jk}^\infty \left(\frac{a^5}{r^7} - \frac{a^3}{r^5}\right) \tag{4.21}$$

$$u_i(x) = u_i^\infty(x_0) + E_{ij}^\infty x_j \left(1 - \frac{a^5}{r^5}\right) + \frac{5}{2} x_i x_j x_k E_{jk}^\infty \left(\frac{a^5}{r^7} - \frac{a^3}{r^5}\right) \tag{4.22}$$

We return to the case for two particles and the previously discussed formulation of the EKF. Each particle will experience the disturbance velocity generated by the motion of the other particle. In this case, the disturbance velocity p that is estimated by the EKF should match the value given Eq. (4.21). The challenge here lies in the fact that p will change with time as the particles move relative to each other, so the EKF must be able to converge quickly to a the value of p. Additionally, the disturbance velocity falls off r^{-2}, so particles must be placed in close proximity to each other so that the estimated value is significant compared to experimental noise.

We simulate this case in MATLAB. Consider two 10 µm diameter particles suspended in a Newtonian fluid. We scale all the quantities using the scaling parameters described in Section 4.2.4. To study interactions between these two particles, we begin by trapping one particle at $\bar{x}_1 = [5, 1.5]^T$ and other particle at the origin ($\bar{x}_2 = 0$). Then while keeping the second particle fixed, the first particle is moved in a sinusoidal motion parallel to the x axis, i.e. $\bar{x}_1 = [5\cos(-10\pi\theta), 1.5]^T$, using the path following algorithm described previously. The parameters for the path following algorithm were $\Phi_{max} = 0.05$, the controller weights were set to $\alpha = 10^3$, $\beta = 10^{-6}$, $\gamma = 10^3$, $\delta_1 = 10^4$ and $\delta_2 = 10^{-6}$, and the error covariances were $Q = I_4$ and $S = 10^{-3}I_4$. Figure 4.8 shows the trajectory of both particles during this manipulation.

In Fig. 4.9 we compare the theoretical prediction of the disturbance velocity to the value obtained from the EKF. As is clear from the figure, we obtain a good agreement between the detected value and the theoretical prediction. Moreover, the interactions estimated for one particle have the same magnitude as interactions sensed by the other particle, but with the opposite sign.

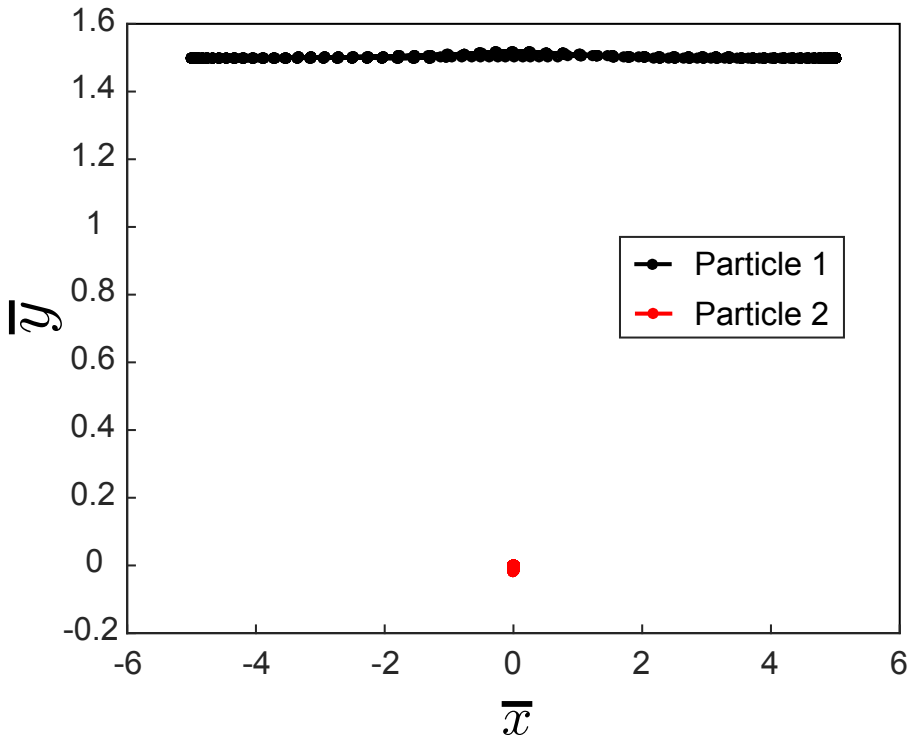

Figure 4.8: The trajectory of both particles during the interaction experiment simulated over a period of 25 seconds. Particle 1 moves in a sinusoidal trajectory parallel to the x axis while Particle 2 is kept fixed at the origin.

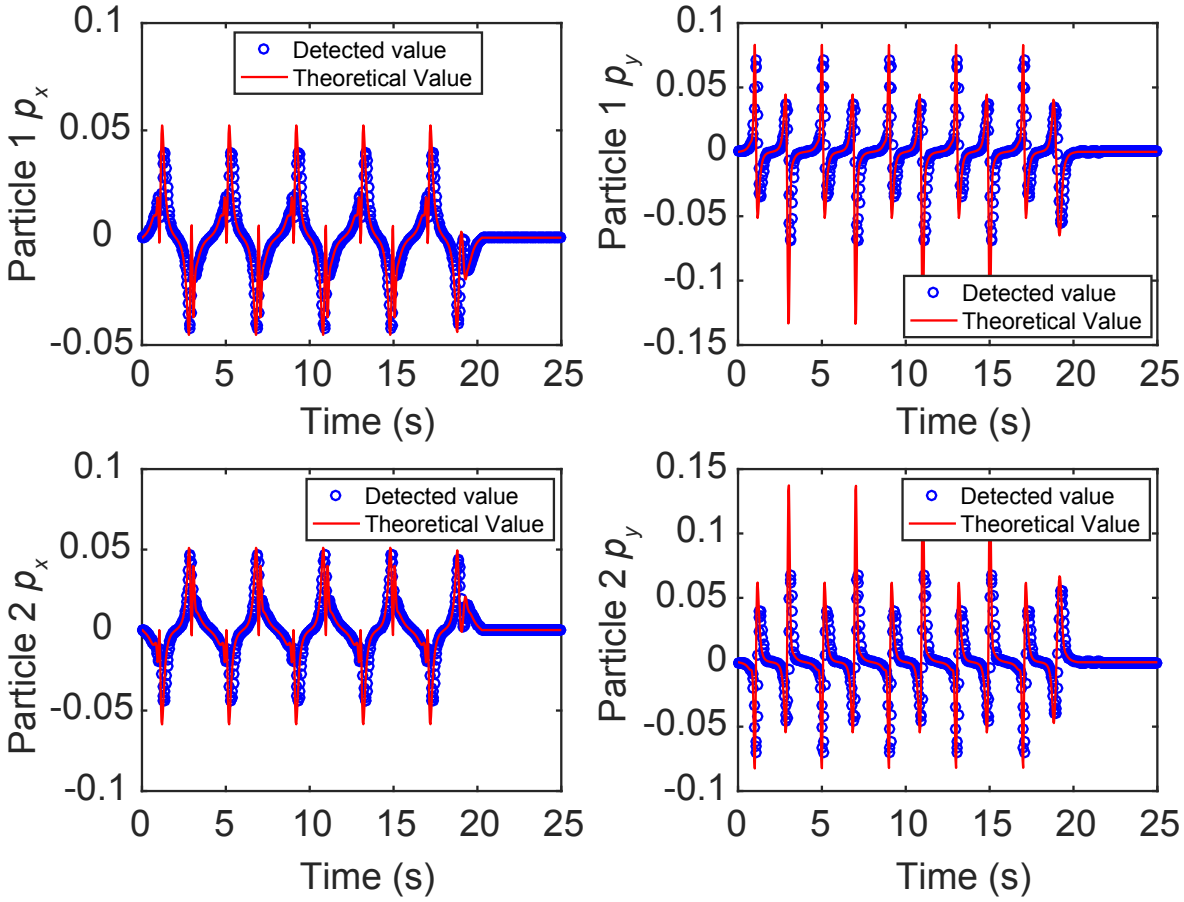

Figure 4.9: A comparison of the theoretical value of the disturbance velocity and the value estimated by the EKF. The EKF estimate shows excellent agreement with the theoretical value.

4.4 Conclusions

In this chapter, we have demonstrated the successful implementation of an extended Kalman filter and a nonlinear model predictive path following control algorithm on the Stokes trap. Typical microfluidic trapping experiments are highly sensitive to incoming disturbances. These disturbances might be extrinsic to the device such as fluctuations in the applied pressure, or intrinsic such as defects in the channel features. Regardless of the source of these disturbances, we need a robust control algorithm which can achieve an offset free regulation of the particle's position. The extended Kalman filter demonstrated here greatly increases the robustness of the controller by estimating the incoming disturbance and removing the offset working in conjunction withe MPC controller. On the other hand, path following allows us even greater flexibility in controlling the precise path followed by a trapped particle. Together, these improvements greatly increase the robustness and the versatility of the Stokes trap.

By combining both of these features together, we also studied hydrodynamic interactions between two particles which are confined using the Stokes trap. By precisely moving one particle along a reference trajectory while keeping the other particle fixed, we were able to use the Kalman filter to directly determine the value of the velocity field induced by the hydrodynamic interactions between the two particles. For Newtonian fluids, the disturbance velocity has an analytical expression which can be readily evaluated. However, for non-Newtonian fluids, the rate-of-strain tensor E_{ij} is no longer linearly related to the stress tensor, which complicates the derivation of the disturbance velocity. The proposed method directly yields the hydrodynamic interaction (i.e., disturbance velocity) between two particles, which does not depend on the shape of the particles or the nature of the surrounding buffer. Thus, this method holds strong potential to enable fundamental studies of interactions between deformable/rigid particles suspended in a wide variety of media.

Chapter 5

Conclusions

In this dissertation, we present several different techniques for flow-mediated particle trapping and manipulation, together with detailed quantitative analysis of these new methods. We began with a systematic analysis of the automated hydrodynamic trap, which uses a heuristic control algorithm to confine particles. We modeled each step of the hydrodynamic trapping process to facilitate a controls-based analysis and simulated the performance of the trap under varying experimental conditions. We defined the oscillations of the particle as a metric for the trap performance, and looked at its variation when the Péclet number, measurement time delay or the system response time was changed. We found that a slow valve or a slow camera leads to poor trapping performance because of larger oscillations of the trapped particle. On the experimental side, we implemented discrete time versions of a proportional (P), proportional-integral (PI) and proportional-integral-derivative (PID) controller. We found that the P and PD controller are the most effective in reducing the oscillations of the particle, and the PI controller is not as effective because it is not able to significantly affect the control action due to the oscillating nature on the error. Although the automated hydrodynamic trap is very effective at confining individual particles, from the perspective of trapping multiple particles, it was handicapped by the complexity of the two layer microfluidic device. Confining multiple particles requires the manipulation of several flow rates which necessitates a complicated microfluidic device with several membrane valves, each of which would possibly have a different deformation behavior upon pressurization.

We further pushed the boundaries of flow-mediated trapping by developing the Stokes trap, which enables confinement and manipulation of an arbitrary number of particles. Moving from a system that could confine a single particle to multiple particles thus required a

substantial redesign of the setup. We approached the problem from the perspective of the degrees of freedom for trapping N particles so we could obtain a solution that was readily scalable. This approach also greatly simplified the design of the microfluidic device, discarding a complicated two layer design in favor of single layer design. By adopting model predictive control and a state space formulation, we were able to formulate the trapping problem in terms of a constrained optimization problem. Recent advances in the computing power of personal computers, as well as algorithmic improvements in the numerical solution of nonlinear optimization problems have made it possible to rapidly solve the high dimensional optimization problem on the microsecond timescale, thus making these control algorithms feasible for trapping micrometer and nanometer sized particles. Using the Stokes trap, we demonstrated a significant increase in the tightness of confinement of a single particle, precise manipulation of two particles along arbitrary paths, as well as the assembly of a simple structure by trapping two sticky particles and bringing them in close proximity. During the trapping experiments, it was observed that unmodeled physics led to an offset between the particle position and the target position. At that time, the objective was only to reject these disturbances, hence we implemented an integrator that was able to reduce this offset to an acceptable value. However, in the case of trapping two particles and bringing them together, this disturbance has information about the hydrodynamic interactions encoded in it, and the integrator does not allow us to extract this information effectively.

The desire to directly measure interactions between particles inspired us to implement an extended Kalman filter (EKF), which processes noisy measurements of the particle position and provides the best estimate of the incoming disturbance conditioned on the previous observations as well as the system model. The EKF was also able to reduce the offset by sharing the most recent estimate of the disturbance with the model predictive controller. We also implemented a path following framework that greatly simplifies the manipulation of particles along arbitrary paths. Here, the motion of the set point is coordinated with the current position of the particle, such that set point preferentially moves at a fast user

defined speed as long as the particle is able to keep up with it, and automatically slows down when the particle lags behind. These two improvements to the Stokes trap led to the development of a novel method to measure hydrodynamic interactions between two freely suspended particles. Essentially, the path following framework is used to precisely move one particle in a sinusoidal motion in the vicinity of the other fixed particle, and the EKF, by continuously observing the discrepancy in either particle's motion, is able to rapidly estimate the velocity field driven by hydrodynamic interactions. This method is agnostic to the morphology and physical properties of the particle as well as the rheological behavior of the suspending medium. Thus, this method enables the measurement of hydrodynamic interactions for a wide variety of particle types.

Moving forward, the Stokes trap holds great promise to enable a multitude of studies in the fields of colloids and soft matter. For instance, the path following framework enables the explicit control of the trajectory of individual particles. In this manner, one could achieve sequential directed assembly, as suggested in a recent publication [31], by introducing sticky particles through distinct channels, and then automatically assemble them into user-defined shapes. The four channel version of the Stokes trap contains an unused degree of freedom when trapping a single particle. This degree of freedom can be exploited to control not only the 2D center of mass position of the particle but also its orientation. By considering the angular relaxation speed of anisotropic particles suspended in a non-Newtonian fluid, it should be possible to infer non-Newtonian rheological properties of the fluid such as the normal stress difference. In the field of soft materials, the ability to directly determine the interactions will enable non-perturbative studies of cell adhesion, vesicle deformation and droplet coalescence.

References

[1] Chu, S, Hollberg, L, Bjorkholm, J. E, Cable, A, & Ashkin, A. (1985) Three-dimensional viscous confinement and cooling of atoms by resonance radiation pressure. *Phys. Rev. Lett.* **55**, 48–51.

[2] Grier, D. G. (2003) A revolution in optical manipulation. *Nature* **424**, 810–816.

[3] Grier, D. G & Roichman, Y. (2006) Holographic optical trapping. *Appl. Opt.* **45**, 880.

[4] Roxworthy, B. J, Ko, K. D, Kumar, A, Fung, K. H, Chow, E. K. C, Liu, G. L, Fang, N. X, & Toussaint, K. C. (2012) Application of Plasmonic Bowtie Nanoantenna Arrays for Optical Trapping, Stacking, and Sorting. *Nano Lett.* **12**, 796–801.

[5] Gosse, C & Croquette, V. (2002) Magnetic Tweezers: Micromanipulation and Force Measurement at the Molecular Level. *Biophys. J.* **82**, 3314–3329.

[6] Mirowski, E, Moreland, J, Zhang, A, Russek, S. E, & Donahue, M. J. (2005) Manipulation and sorting of magnetic particles by a magnetic force microscope on a microfluidic magnetic trap platform. *Appl. Phys. Lett.* **86**, 243901.

[7] Cohen, A. E & Moerner, W. E. (2005) Method for trapping and manipulating nanoscale objects in solution. *Appl. Phys. Lett.* **86**, 093109.

[8] Cohen, A. E & Moerner, W. E. (2006) Suppressing Brownian motion of individual biomolecules in solution. *Proc. Natl. Acad. Sci. U.S.A.* **103**, 4362–4365.

[9] Cohen, A. E & Moerner, W. E. (2008) Controlling Brownian motion of single protein molecules and single fluorophores in aqueous buffer. *Opt. Express* **16**, 6941.

[10] Probst, R, Cummins, Z, Ropp, C, Waks, E, & Shapiro, B. (2012) Flow Control of Small Objects on Chip: Manipulating Live Cells, Quantum Dots, and Nanowires. *IEEE Control Syst.* **32**, 26–53.

[11] Cummins, Z, Probst, R, & Shapiro, B. (2013) Electrokinetic tweezing: three-dimensional manipulation of microparticles by real-time imaging and flow control. *Lab. Chip* **13**, 4040–4046.

[12] Hertz, H. M. (1995) Standing-wave acoustic trap for nonintrusive positioning of microparticles. *J. Appl. Phys.* **78**, 4845–4849.

[13] Ding, X, Lin, S.-C. S, Kiraly, B, Yue, H, Li, S, Chiang, I.-K, Shi, J, Benkovic, S. J, & Huang, T. J. (2012) On-chip manipulation of single microparticles, cells, and organisms using surface acoustic waves. *Proc. Natl. Acad. Sci. U.S.A.* **109**, 11105–11109.

[14] Tanyeri, M, Johnson-Chavarria, E. M, & Schroeder, C. M. (2010) Hydrodynamic trap for single particles and cells. *Appl. Phys. Lett.* **96**, 224101.

[15] Tanyeri, M, Ranka, M, Sittipolkul, N, & Schroeder, C. M. (2011) A microfluidic-based hydrodynamic trap: design and implementation. *Lab. Chip* **11**, 1786.

[16] Tanyeri, M & Schroeder, C. M. (2013) Manipulation and Confinement of Single Particles Using Fluid Flow. *Nano Lett.* **13**, 2357–2364.

[17] Shenoy, A, Tanyeri, M, & Schroeder, C. M. (2015) Characterizing the performance of the hydrodynamic trap using a control-based approach. *Microfluid. Nanofluid.* **18**, 1055–1066.

[18] Shenoy, A, Rao, C. V, & Schroeder, C. M. (2016) Stokes trap for multiplexed particle manipulation and assembly using fluidics. *Proc. Natl. Acad. Sci. U.S.A.* **113**, 3976–3981.

[19] Vorobjev, I. A, Liang, H, Wright, W. H, & Berns, M. W. (1993) Optical trapping for chromosome manipulation: a wavelength dependence of induced chromosome bridges. *Biophys. J.* **64**, 533–538.

[20] Cohen, A. E & Moerner, W. E. (2007) Principal-components analysis of shape fluctuations of single DNA molecules. *Proceedings of the National Academy of Sciences* **104**, 12622–12627.

[21] Peterman, E. J. G, Gittes, F, & Schmidt, C. F. (2003) Laser-Induced Heating in Optical Traps. *Biophys. J.* **84**, 1308–1316.

[22] Taylor, G. I. (1934) The Formation of Emulsions in Definable Fields of Flow. *Proc. R. Soc. A* **146**, 501–523.

[23] Bentley, B. J & Leal, L. G. (1986) A computer-controlled four-roll mill for investigations of particle and drop dynamics in two-dimensional linear shear flows. *J. Fluid Mech.* **167**, 219–240.

[24] Schroeder, C. M, Babcock, H. P, Shaqfeh, E. S. G, & Chu, S. (2003) Observation of Polymer Conformation Hysteresis in Extensional Flow. *Science* **301**, 1515–1519.

[25] Schroeder, C. M, Shaqfeh, E. S. G, & Chu, S. (2004) Effect of Hydrodynamic Interactions on DNA Dynamics in Extensional Flow: Simulation and Single Molecule Experiment. *Macromolecules* **37**, 9242–9256.

[26] Hudson, S. D, Jr, F. R. P, Handler, M. D, Cabral, J. T, Migler, K. B, & Amis, E. J. (2004) Microfluidic analog of the four-roll mill. *Appl. Phys. Lett.* **85**, 335–337.

[27] Lee, J. S, Dylla-Spears, R, Teclemariam, N. P, & Muller, S. J. (2007) Microfluidic four-roll mill for all flow types. *Appl. Phys. Lett.* **90**, 074103.

[28] Curtis, M. D, Sheard, G. J, & Fouras, A. (2011) Feedback control system simulator for the control of biological cells in microfluidic cross slots and integrated microfluidic systems. *Lab. Chip* **11**, 2343–2351.

[29] Tanyeri, M, Ranka, M, Sittipolkul, N, & Schroeder, C. M. (2011) Microfluidic Wheatstone bridge for rapid sample analysis. *Lab. Chip* **11**, 4181–4186.

[30] Moyle, T. M, Walker, L. M, & Anna, S. L. (2013) Controlling thread formation during tipstreaming through an active feedback control loop. *Lab. Chip* **13**, 4534–4541.

[31] Schneider, T. M, Mandre, S, & Brenner, M. P. (2011) Algorithm for a Microfluidic Assembly Line. *Phys. Rev. Lett.* **106**, 094503.

[32] Batchelor, G. K. (2000) *An Introduction to Fluid Dynamics*. (Cambridge University Press, Cambridge).

[33] Mayne, D. Q, Rawlings, J. B, Rao, C. V, & Scokaert, P. O. (2000) Constrained model predictive control: Stability and optimality. *Automatica* **36**, 789–814.

[34] Houska, B, Ferreau, H. J, & Diehl, M. (2011) ACADO toolkitâĂŤAn open-source framework for automatic control and dynamic optimization. *Optim. Control Appl. Methods* **32**, 298–312.

[35] Houska, B, Ferreau, H. J, & Diehl, M. (2011) An auto-generated real-time iteration algorithm for nonlinear MPC in the microsecond range. *Automatica* **47**, 2279–2285.

[36] Quirynen, R, Vukov, M, Zanon, M, & Diehl, M. (2015) Autogenerating microsecond solvers for nonlinear MPC: A tutorial using ACADO integrators. *Optim. Control Appl. Methods* **36**, 685–704.

[37] Sbalzarini, I. F & Koumoutsakos, P. (2005) Feature point tracking and trajectory analysis for video imaging in cell biology. *J. Struct. Biol.* **151**, 182–195.

[38] Lansdorp, B. M & Saleh, O. A. (2012) Power spectrum and Allan variance methods for calibrating single-molecule video-tracking instruments. *Rev. Sci. Instrum.* **83**.

[39] Yu, Z, Dulin, D, Cnossen, J, KÃűber, M, Oene, M. M. v, Ordu, O, Berghuis, B. A, Hensgens, T, Lipfert, J, & Dekker, N. H. (2014) A force calibration standard for magnetic tweezers. *Rev. Sci. Instrum.* **85**, 123114.

[40] Neuman, K. C & Nagy, A. (2008) Single-molecule force spectroscopy: optical tweezers, magnetic tweezers and atomic force microscopy. *Nat. Methods* **5**, 491–505.

[41] Pozrikidis, C. (1992) *Boundary Integral and Singularity Methods for Linearized Viscous Flow*. (Cambridge University Press, Cambridge).

[42] Leal, L. G. (2007) *Advanced transport phenomena: fluid mechanics and convective transport processes*. (Cambridge University Press, Cambridge).

[43] Chiou, P. Y, Ohta, A. T, & Wu, M. C. (2005) Massively parallel manipulation of single cells and microparticles using optical images. *Nature* **436**, 370–372.

[44] Hecht, S. (2005) Construction with macromolecules. *Mater. Today* **8**, 48–55.

[45] Whitesides, G. M & Boncheva, M. (2002) Beyond molecules: Self-assembly of mesoscopic and macroscopic components. *Proc. Natl. Acad. Sci. U.S.A.* **99**, 4769–4774.

[46] Syms, R, Yeatman, E, Bright, V, & Whitesides, G. M. (2003) Surface tension-powered self-assembly of microstructures - the state-of-the-art. *J. Microelectromech. Syst.* **12**, 387–417.

[47] Meng, G, Arkus, N, Brenner, M. P, & Manoharan, V. N. (2010) The Free-Energy Landscape of Clusters of Attractive Hard Spheres. *Science* **327**, 560–563.

[48] Vijayaraghavan, A, Blatt, S, Weissenberger, D, Oron-Carl, M, Hennrich, F, Gerthsen, D, Hahn, H, & Krupke, R. (2007) Ultra-Large-Scale Directed Assembly of Single-Walled Carbon Nanotube Devices. *Nano Lett.* **7**, 1556–1560.

[49] Bevan, M. A, Ford, D. M, Grover, M. A, Shapiro, B, Maroudas, D, Yang, Y, Thyagarajan, R, Tang, X, & Sehgal, R. M. (2015) Controlling assembly of colloidal particles into structured objects: Basic strategy and a case study. *J. Process Control* **27**, 64–75.

[50] Xu, F, Finley, T. D, Turkaydin, M, Sung, Y, Gurkan, U. A, Yavuz, A. S, Guldiken, R, & Demirci, U. (2011) The Assembly of Cell-Encapsulating Microscale Hydrogels Using Acoustic Waves. *Biomaterials* **32**, 7847–7855.

[51] Pantina, J. P & Furst, E. M. (2004) Directed Assembly and Rupture Mechanics of Colloidal Aggregates. *Langmuir* **20**, 3940–3946.

[52] Zhang, H & Liu, K.-K. (2008) Optical tweezers for single cells. *J. R. Soc. Interface* **5**, 671–690.

[53] Maybeck, P. S. (1982) *Stochastic models, estimation, and control.* (Academic press) Vol. 3.

[54] Faulwasser, T, Weber, T, Zometa, P, & Findeisen, R. (2016) Implementation of nonlinear model predictive path-following control for an industrial robot. *IEEE Trans. Control Syst. Technol.*